# Robust control of q-profile and $\beta$p using data-driven models on EAST

Sen Wang, Emmanuel Witrant, Didier Moreau

HAL Id: hal-03097933
https://hal.univ-grenoble-alpes.fr/hal-03097933

Submitted on 2 Jan 2023

# Robust control of q-profile and $\beta_p$ using data-driven models on EAST

S. Wang[1], E. Witrant[1], D. Moreau[2]

[1] *Université Grenoble Alpes, CNRS, GIPSA-lab, 38000 Grenoble, France*

[2] *CEA, IRFM, 13108 Saint-Paul-lez-Durance, France*

**Abstract**

A new robust feedback controller for the safety factor profile and poloidal plasma pressure parameter has been developed using a two-time-scale data-driven model. The model describes the linear plasma responses of the $\iota$ profile and $\beta_p$ with respect to auxiliary heating & current drive (H&CD) powers, around a typical plasma equilibrium in an H-mode steady-state plasma discharge on EAST. The feedback controller comprises a carefully designed low-pass filter for the timescale separation, a decoupling module and three local controllers synthesized from the $\mathcal{H}_\infty$ norm optimization and the singular value decomposition. The actuators are the lower hybrid current drive (LHCD) system at 4.6 GHz and the ion cyclotron resonance heating (ICRH) system at 33 MHz. Taking into account the actuation dynamics, an anti-windup technique is employed to condition the controller online aiming to attenuate the negative effects from moderate time delays and power saturations. Extensive nonlinear closed-loop simulations with the METIS code suggest that high $\beta_p$ and negative central magnetic shear that characterize advanced tokamak plasma scenarios can be achieved and sustained on EAST with good tracking performance and reasonable robustness via the proposed control scheme. The feedback control of the core $\iota$ profile and $\beta_p$ with a range of time delays, power saturations and varying weighting functions are evaluated numerically, compared and discussed. The control robustness to plasma parameter uncertainties including the line-averaged plasma density $\langle \bar{n}_e \rangle$, the H-mode enhancement factor $H_{\text{factor}}$ and the effective charge number $Z_{\text{eff}}$ are assessed and analyzed.

*Keywords:* EAST, Plasma control, Robust control, q-profile, $\beta_p$

*2020 MSC:* 00-01, 99-00

## 1. Introduction

One of the main challenges for the tokamak plasma operation is to achieve and maintain advanced plasma scenarios with high plasma pressures and temperatures so that a high gain nuclear fusion burn can be sustained. However, since a series of magnetohydrodynamic (MHD) instabilities and microturbulence commonly exist in various locations and phases of tokamak plasmas that may deteriorate plasma confinement and even lead to disruptions[1], it is demanding to deliver and sustain advanced tokamak plasma scenarios without active feedback control.

Among numerous tokamak plasma parameters, the safety factor $q$ is defined as the rate of change of toroidal flux with poloidal flux, i.e., $q = -\frac{d\Phi}{d\Psi}$, a particularly important parameter whose shape and magnitude are directly associated with some deleterious MHD events and micro-instabilities [2, 3]. For instance, sawtooth crashes occur when the plasma safety factor is less than 1 [4]; Neoclassical tearing modes (NTM's) appear and grow around plasma flux surfaces where the safety factor has rational values such as 3/2 and 2/1 [5]. Moreover, it is inferred that the negative central magnetic shear ($s = \frac{r}{q}\frac{\partial q}{\partial r}$) is an important stabilizing factor to reduce turbulence transport in the pressure gradient region, thus supporting the formation of ion/electron internal transport barriers (i/eITB's) [6, 7]. In view of the different time scales involved in plasma dynamics, simultaneous control of the q-profile and kinetic parameters (e.g. the stored energy, W, the normalized pressure parameter, $\beta_N$, or the poloidal pressure parameter, $\beta_p$) is preferred to the control of the safety factor profile alone [8, 9]. In this work, the simultaneous control of q-profile and $\beta_p$ is investigated. $\beta_p$ is a ratio between the total plasma kinetic energy and the energy stored in the poloidal magnetic field, which is expressed as $\beta_p = \frac{4W(1+\kappa^2)}{3\mu_0 a R I_p^2}$, where $W$ represents the plasma kinetic energy, $\kappa$ the elongation, $\mu_0$ the magnetic permeability in vacuum space, $a$ the minor radius, $R$ the major radius, $I_p$ plasma current.

Various control schemes have been pursued both numerically and experimentally on different tokamaks, for example, DIII-D [8, 10, 11, 12, 13], NSTX-U [14, 15, 16], TCV [17, 18, 19, 20, 21] and JET [22, 23, 24]. Many of the control schemes are based on the first-principle-based physical models [25], while others are synthesized by using data-driven models identified from dedicated experimental and/or simulation data. In this study, data-driven models are utilized for feedback control design because we advert that the transport physics for high confinement plasma has not been fully clarified such that many essential physical parameters are estimated empirically via scaling laws. First-principle-based models appear to be more difficult to generally describe the

2

multi-scale plasma dynamics in advanced plasma scenarios, especially in terms of fast timescale kinetic evolutions. In view of these, [22, 26, 27] proposed a semi-empirical data-driven modelling approach that depicts the response of magnetic and kinetic profiles to the variations of the heating and current drive (H&CD) actuators using linear two-time-scale models whose structure is based on the first-order singular perturbation expansion of the MHD equations governing plasma dynamics. However, the actual evolutions of magnetic and kinetic profiles in tokamak plasmas are basically non-linear, which necessitates data-driven model-based control to be sufficiently robust against model uncertainties and possible parameter disturbances. Therefore, in this work, we propose a new data-driven model-based robust control scheme by combining the multivariate $\mathcal{H}_\infty$ norm optimal control with the singular perturbation theory and demonstrate its effectiveness in both control performance and robustness via extensive nonlinear closed-loop simulations for an EAST H-mode steady-state scenario with the METIS code [28].

Due to its simplicity and robustness properties, the $\mathcal{H}_\infty$ optimal control technique has been applied to various tokamak plasma control problems.In [13, 10], an $\mathcal{H}_\infty$ optimal controller combined with a feedforward optimizer synthesized from first-principles-driven models has been applied to track the trajectories of the poloidal flux gradient profile in L-mode and H-mode plasma scenarios on DIII-D experimentally. In [29], a robust proportional-integral-derivative (PID) control technique using data-driven models is employed to stabilize the vertical instability on the WEST tokamak numerically. In [30], the similar technique has been extended to control the poloidal field coil currents, plasma position and shape parameters on WEST experimentally. In [31], the averaged electron density was successfully controlled by actuating a gas valve, based on $\mathcal{H}_\infty$ robust feedback synthesis on the TCV tokamak.

Although using the $\mathcal{H}_\infty$ optimal control technique is not new, the $\mathcal{H}_\infty$ controller that we propose here is based on the principles of the timescale separation and the direct online control decoupling via vector analysis. The second contribution is to consider the actuators dynamics, where an extra closed-loop is involved to deal with the negative effects from moderate actuation time delays and power saturations. We also propose three general performance indexes to characterize the plasma current profile control performance and are applied to performance comparison and analysis. In terms of controller tuning, we provide, for the first time, a direct numerical verification of the effects of control tuning parameters in robust synthesis on the plasma current profile control performance via extensive nonlinear closed-loop simulations. Using this robust control scheme,

3

H-mode steady-state scenarios are conveniently exploited and valuable indications on the H-mode steady-state scenario development are summarised. Techniques on the control initialization and setpoint selections are also highlighted, which play a non-negligible role in the control of q-profile and $\beta_p$.

The remainder of the paper is organized as follows: the two-time-scale plasma model is briefly described in Section 2. In Section 3 $\mathcal{H}_\infty$ feedback control controller is synthesized from the data-driven model and beneficial control implementation techniques are presented. Section 4 aims to numerically evaluate the effectiveness of the robust control scheme via extensive nonlinear closed-loop simulations for H-mode steady state plasma scenarios on EAST with the METIS code. Finally, we draw conclusions and suggest possible extensions of this work.

## 2. Two-time-scale Plasma Model

In tokamak plasmas, there are multiple time scales in which various parameters/profiles evolve [1]. Specifically, the inversed safety factor profile has much slower dynamics than plasma pressure in medium-sized (e.g. EAST) and large tokamaks (e.g. ITER). By virtue of this, we describe the coupled dynamics of $\iota$, defined as an inverse of the safety factor $q$, and $\beta_p$ in a two-time-scale manner, linearized around a plasma equilibrium [22, 26, 27]. The model reads as:

$$
\begin{bmatrix} \frac{\partial \Psi(x,t)}{\partial t} \\ \epsilon \frac{\partial \Xi(x,t)}{\partial t} \end{bmatrix} = \begin{bmatrix} M_{\Psi,\Psi}(x) & M_{\Psi,\Xi}(x) \\ M_{\Xi,\Psi}(x) & M_{\Xi,\Psi}(x) \end{bmatrix} \begin{bmatrix} \Psi(x,t) \\ \Xi(x,t) \end{bmatrix} + \begin{bmatrix} M_{\Psi,U}(x) \\ M_{\Xi,U}(x) \end{bmatrix} U(t)
$$

(1)

where $x$, namely the flux-averaged normalized radius, is defined as $(\Phi/\Phi_{max})^{1/2}$ , in which $\Phi(x)$ is the toroidal magnetic flux within a given flux surface, and $\Phi_{max}$ is the maximum value at the last closed flux surface (LCFS). $\Psi(x,t)$ represents the poloidal magnetic flux minus its value at the plasma boundary, while $\Xi(x,t)$ a combination of kinetic parameters/profiles. $U(t)$ is a vector of actuators containing the heating and current drive powers. The constant $\epsilon$ denotes a typical value of the ratio between the kinetic and magnetic time constants, which makes the various elements of the $M$ matrix of comparable magnitude.

In order to obtain finite dimensional variables for control design, a projection of Eq. (1) onto cubic spline basis functions is carried out. For the EAST tokamak, $\epsilon$ is typically 0.05, hence a

singular perturbation approach is employed. Then the linearized PDE is transformed into a two-time-scale state space model as described below.

Defining:

$$\Xi(t) = \Xi_S(t) + \Xi_F(t), U(t) = U_S(t) + U_F(t) \tag{2}$$

The slow model is:

$$\dot{\Psi}(t) = A_S \Psi(t) + B_S U_S(t)$$
$$\Xi_S(t) = C_S \Psi(t) + D_S U_S(t) \tag{3}$$

while the fast model is:

$$\dot{\Xi}_F(t) = A_F \Xi_F(t) + B_F U_F(t) \tag{4}$$

Where $\Xi(t)$ is a vector of kinetic variables, comprising the slow $\Xi_S$ and fast $\Xi_F$ components. Likewise, $U(t)$ is a vector of actuated powers with the slow part $U_S(t)$ and fast part $U_F(t)$.

The control of $\iota$-profile motivates us to model the $\iota$-profile dynamics. $\iota(\rho, t)$ is defined as

$$\iota(\rho, t) = -\frac{d\Psi(\rho, t)}{d\Phi(\rho, t)} = -\frac{\partial \Psi(\rho, t)}{\partial \rho}\frac{\partial \rho}{\partial \Phi(\rho, t)} = -\frac{\pi}{\Phi_{max}(t)}\left(\frac{1}{\rho}\frac{\partial \Psi(\rho, t)}{\partial \rho}\right) \tag{5}$$

Linearizing $\iota(\rho, t)$ around a reference profile $\iota_{ref}(\rho)$, projecting $\iota(\rho, t)$ on the cubic basis functions, we then obtain

$$\tilde{\iota}(t) = C_\iota \Psi(t), \quad \tilde{\iota}(t) = \iota(t) - \bar{\iota} \tag{6}$$

where $\tilde{\iota}$ are a vector of the perturbed $\iota$ profile around a reference profile $\bar{\iota}$. $C_\iota$ is a constant coefficient matrix by assuming the constant $\Phi_{max}$, which is satisfied when the plasma shape parameters and the toroidal magnetic fields remain constant. Combining the equations (2), (3), (4) and (6), we derive the two-time-scale plasma response model that desribes the $\iota$-profile and kinetic parameter dynamics in a structural form.

In this work, the objective is to acquire the response of $\iota$ and $\beta_p$ to actuated powers from the ion cyclotron resonance heating (ICRH) and lower hybrid current drive (LHCD) systems for an H-mode EAST plasma at the flat-top phase, in which $\iota$ is a vector evolving only at the magnetic timescale, uniformly distributed in 10 points, i.e. $x = 0, 0.1, 0.2, ..., 0.9$, while $\beta_p$ is a scalar evolving both at the magnetic and kinetic timescales. Specifically, the model for $\iota$ and $\beta_p$ is given as follows.

The slow model is:

$$
\begin{bmatrix} \dot{\Psi}_0(t) \\ \dot{\Psi}_1(t) \\ ... \\ \dot{\Psi}_{N-1}(t) \end{bmatrix} = A_\Psi \begin{bmatrix} \Psi_0(t) \\ \Psi_1(t) \\ ... \\ \Psi_{N-1}(t) \end{bmatrix} + B_\Psi \begin{bmatrix} U_{S,IC}(t) \\ U_{S,LH}(t) \end{bmatrix}, N = 10 \tag{7}
$$

$$
\begin{bmatrix} \iota_0(t) \\ \iota_1(t) \\ ... \\ \iota_{N-1}(t) \\ \beta_{p,S}(t) \end{bmatrix} = \begin{bmatrix} C_\iota \\ C_{\beta_{p,S}} \end{bmatrix} \begin{bmatrix} \Psi_0(t) \\ \Psi_1(t) \\ ... \\ \Psi_{N-1}(t) \end{bmatrix} + \begin{bmatrix} D_\iota \\ D_{\beta_{p,S}} \end{bmatrix} \begin{bmatrix} U_{S,IC} \\ U_{S,LH} \end{bmatrix} \tag{8}
$$

while the fast model is:

$$
\dot{\beta}_{p,F}(t) = A_{\beta_p,F}\beta_{p,F}(t) + B_{\beta_p,F} \begin{bmatrix} U_{F,IC} \\ U_{F,LH} \end{bmatrix} \tag{9}
$$

and the controlled input is decomposed as:

$$
\begin{bmatrix} U_{IC} \\ U_{LH} \end{bmatrix} = \begin{bmatrix} U_{S,IC} \\ U_{S,LH} \end{bmatrix} + \begin{bmatrix} U_{F,IC} \\ U_{F,LH} \end{bmatrix} \tag{10}
$$

## 3. Control Design

In this section, we present the robust feedback design using the two-time-scale model. First we describe the overall control scheme. Then details of the feedback synthesis are illustrated, including the control-oriented model formulation, local controllers design, the control decoupling and some remarks on controller tunings. Subsequently, we introduce beneficial control implementation techniques to guarantee the performance and robustness of the proposed controller both in nonlinear closed-loop simulations and in real-time tokamak plasma control experiments.

In order to design a robust feedback controller that possesses sufficient freedom, available for control of $\iota$ and $\beta_p$ both separately and simultaneously (with multi-function), feedback controllers with different control objectives are synthesized separately and then being integrated for composite control. As depicted in Fig. 1, the controller is divided into two components: feedforward and feedback. The feedforward component is a simple module involving constant H&CD powers at
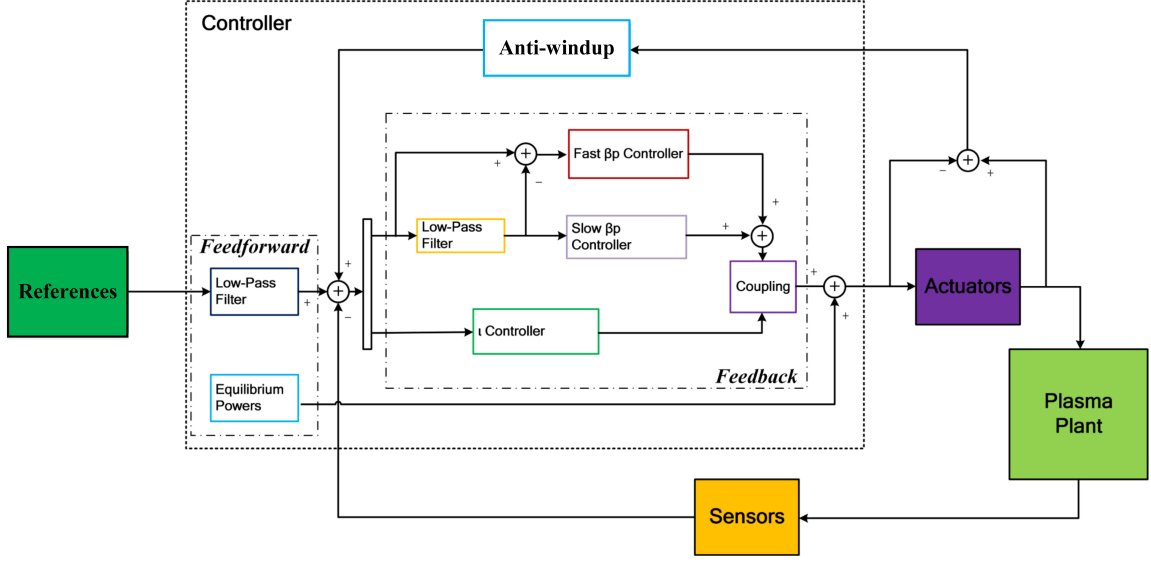
6

Figure 1: Feedback-feedforward control scheme for $\iota$ and $\beta_p$ using timescales separation

the plasma equilibrium around which the model is linearized, and a low-pass filter with two time constants for the $\beta_p$ and $\iota$ respectively to make the reference trajectories smooth. The feedback component consists of a low-pass filter, three local controllers and a decoupling module. The low-pass filter in the feedback component, with a time constant between kinetic and magnetic timescales, is designed to split the $\beta_p$ estimation into the fast and slow components such that the fast one is controlled by the fast $\beta_p$ controller in the kinetic timescale, while the slow one is controlled by the slow $\beta_p$ controller in the magnetic timescale. The $\iota$ controller is designed separately using the slow model for $\iota$. The decoupling module is employed to formulate the simultaneous control of $\iota$ and $\beta_p$. The control conditioning module is involved to attenuate the negative effects from moderate actuation time delays and power saturations.

### 3.1. Feedback synthesis

The feedback control objective is to minimize tracking errors from any reference inputs, attenuate the effects from system disturbances as well as involve minimum control efforts. The definition of gain for a transfer function matrix (or in terms of a state-space representation) is given by its singular values [32]. By shaping the singular values of appropriately specified transfer function matrices, the closed-loop control performance can therefore be guaranteed. As shown in Fig. 2(a), the
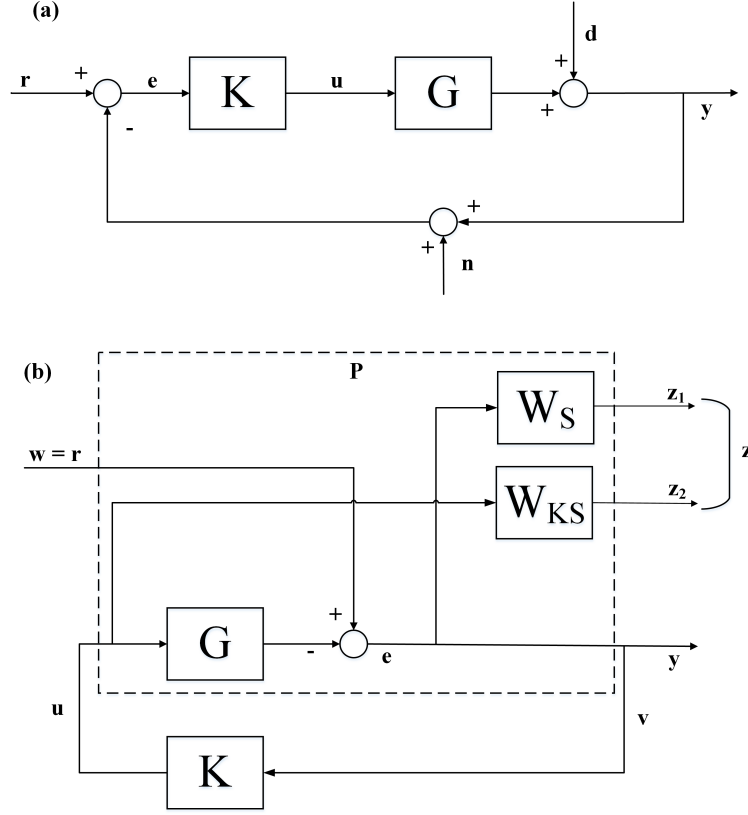
7

Figure 2: Schematic of the $\mathcal{H}_\infty$ norm feedback control formulation

plant $G$ and the controller $K$ interconnection is driven by reference inputs $r$, output disturbances $d$ and measurement noise $n.y$ are the controlled variables while $u$ represent the controlled inputs. The sensitivity function is then expressed as $S = (I + GK)^{-1}$, which expresses the mapping from $y/r/d$ to the control error $e$. The transfer function $KS$ represents the mapping from $y/r/d$ to $u$. Shaping the maximum singular value of $S$ and $KS$ in the frequency domain can then be transformed into minimizing the $\mathcal{H}_\infty$ norm of the integrated transfer function matrix $\begin{bmatrix} W_S S & W_{KS} KS \end{bmatrix}$, where $W_S$ and $W_{KS}$ are appropriately designed weighting functions for $S$ and $KS$, respectively. Therefore, the feedback control synthesis problem is formulated as an $\mathcal{H}_\infty$ norm optimization problem, which is easily solved by using linear matrix inequalities (LMIs).

8

*3.1.1. Solving $\mathcal{H}_\infty$ norm optimization problem using LMIs*

We consider a general state-space model $G = (A_0, B_0, C_0, D_0)$. As shown in Fig. 2(b), the weighting functions $W_S = (A_S, B_S, C_S, D_S)$ and $W_{KS} = (A_{KS}, B_{KS}, C_{KS}, D_{KS})$ are respectively interconnected to the feedback control error $e$ and the controlled input $u$ with the combined output as $z$. The controller is realized as $K = (A_c, B_c, C_c, D_c)$ with the input as $y$ and the output as $u$. The reference inputs $r$, the output disturbances $y$ and noise $n$ are considered as $w$. We then augment the plant model $G$ into a generalized linear time-invariant (LTI) state-space form $P$ as:

$$
\begin{bmatrix} \dot{x} \\ \hline z \\ y \end{bmatrix} = \left[ \begin{array}{c|cc} A & B_1 & B_2 \\ \hline C_1 & D_{11} & D_{12} \\ C_2 & D_{21} & D_{22} \end{array} \right] \begin{bmatrix} x \\ \hline w \\ u \end{bmatrix}
\tag{11}
$$

where

$$
A = \begin{bmatrix} A_0 & 0 & 0 \\ -B_S C_0 & A_S & 0 \\ 0 & 0 & A_{KS} \end{bmatrix}, B_1 = \begin{bmatrix} 0 \\ B_S \\ 0 \end{bmatrix}, B_2 = \begin{bmatrix} B_0 \\ -B_S D_0 \\ B_{KS} \end{bmatrix}, C_1 = \begin{bmatrix} -D_S C_0 & C_S & 0 \\ 0 & 0 & C_{KS} \end{bmatrix}
$$

$$
C_2 = \begin{bmatrix} C_0 & 0 & 0 \end{bmatrix}, D_{11} = \begin{bmatrix} D_S \\ 0 \end{bmatrix}, D_{12} = \begin{bmatrix} -D_S D_0 \\ D_{KS} \end{bmatrix}, D_{21} = 0, D_{22} = D_0
$$

and $x$ is the state vector of the plant $G$ plus the state vector of the weighting functions $W_S$ and $W_{KS}$. We assume that $x \in X \subset \mathbb{R}^n$, $z \in Z \subset \mathbb{R}^{n_z}$, $y \in Y \subset \mathbb{R}^{n_y}$, $w \in W \subset \mathbb{R}^{n_w}$ and $u \in U \subset \mathbb{R}^{n_u}$. In order to synthesize the robust feedback controller $K$ for the plant $G$, the following theorem is applied.

**Theorem 1.** *(Scherer et al., 1997 [33]). A dynamical output feedback controller $K : (A_c, B_c, C_c, D_c)$ with $n_u$ outputs and $n_y$ inputs that solves the $\mathcal{H}_\infty$ norm problem is obtained by solving the following LMIs in $(X, Y, \tilde{A}, \tilde{B}, \tilde{C}, \tilde{D})$ while minimizing $\gamma$:*

$$\begin{bmatrix} M_{11} & (*)^T & (*)^T & (*)^T \\ M_{21} & M_{22} & (*)^T & (*)^T \\ M_{31} & M_{32} & M_{33} & (*)^T \\ M_{41} & M_{42} & M_{43} & M_{44} \end{bmatrix} < 0 \tag{12}$$

$$\begin{bmatrix} X & I_n \\ I_n & Y \end{bmatrix} > 0$$

where

$$M_{11} = AX + XA^T + B_2\tilde{C} + \tilde{C}^T B_2^T$$

$$M_{21} = \tilde{A} + A^T + C_2^T \tilde{D}^T B_2^T$$

$$M_{22} = YA + A^TY + \tilde{B}C_2 + C_2^T \tilde{B}^T$$

$$M_{31} = B_1^T + D_{21}^T \tilde{D}^T B_2^T$$

$$M_{32} = B_1^TY + D_{21}^T \tilde{B}^T;$$

$$M_{33} = -\gamma I_{n_u}$$

$$M_{41} = C_1X + D_{12}\tilde{C}$$

$$M_{42} = C_1 + D_{12}\tilde{D}C_2$$

$$M_{43} = D_{11} + D_{12}\tilde{D}D_{21}$$

$$M_{44} = -\gamma I_{n_y}$$

Then, the dynamical feedback controller $K$ is given in the state space form with state-space matrices:

$$D_c = \tilde{D}$$

$$C_c = (\tilde{C} - D_cC_2X)M^{-T}$$

$$B_c = N^{-1}(\tilde{B} - YB_2D_c) \tag{13}$$

$$A_c = N^{-1}(\tilde{A} - YAX - YB_2D_cC_2X$$

$$\quad - NB_cC_2X - YB_2C_cM^T)M^{-T}$$

where M and N are such that $MN^T = I_n - XY$.

In order to apply the above theorem to solving the $\mathcal{H}_\infty$ norm optimization problem and synthesize a robust feedback controller that satisfies the feedback control objective, the two-time-scale model derived in Section 2, i.e. equations (2)-(4) and (6), is reformulated as three sub-models which are expressed in the state-space form as:

$$
G_{\beta_{p,F}} = \left[ \begin{array}{c|c} A_{\beta_p,F} & B_{\beta_p,F} \\ \hline 1 & 0 \end{array} \right]
$$

$$
G_{\beta_{p,S}} = \left[ \begin{array}{c|c} A_\Psi & B_\Psi \\ \hline C_{\beta_p,S} & D_{\beta_p,S} \end{array} \right] \tag{14}
$$

$$
G_\iota = \left[ \begin{array}{c|c} A_\Psi & B_\Psi \\ \hline C_\iota & D_\iota \end{array} \right]
$$

where $G_{\beta_{p,F}}$, $G_{\beta_{p,S}}$ and $G_\iota$ respectively represent the fast $\beta_p$ model, the slow $\beta_p$ model and the $\iota$ model. The three models are considered as three plants and are utilized for local controllers design.

### 3.1.2. Local controllers design

In this subsection, we design three local controllers for the fast and slow $\beta_p$ control as well as $\iota$ control. The design procedure is illustrated in Fig. 3.

The fast $\beta_p$ controller is synthesized by shaping the mixed-sensitivity functions of the fast $\beta_p$ model. Since the number of controlled variables is less than that of actuators, a singular value decomposition (SVD) technique is employed on the fast $\beta_p$ model at a cut-off frequency $\omega_{c,\beta_p,F}$ to extract the principal output and input control channels, expressed as $G_1 = W_1 \Sigma_1 V_1^T$, where $G_1 = (\omega_{c,\beta_p,F} I - A_{\beta_p,F})^{-1} B_{\beta_p,F}$. The cut-off frequency $\omega_{c,\beta_p,F}$ represents the lower closed-loop bandwidth for the fast $\beta_p$ controller, which is set at 1 rad/s. $W_1$ are the left singular vectors, $V_1$ are the right singular vectors, $\Sigma_1$ the diagonal matrix with singular values of $G_1$ on its diagonal. Assume the first left and right singular vectors as well as the first singular value to be $W_{1,1}$, $V_{1,1}$ and $\Sigma_{1,1}$, respectively, which represent the principal control channel for the fast $\beta_p$ dynamics. Projecting $G_{\beta_{p,F}}$ onto the principal output and input control channels yields $G_{\beta_p,F,1} = W_{1,1} G_{\beta_{p,F}} V_{1,1} \Sigma_{1,1}^{-1}$. Assume that $K_{\beta_p,F,1}$ represents the transfer function of the controller for the plant model $G_{\beta_p,F,1}$, and then the sensitivity function $S_{\beta_p,F,1}$ is derived as $(1 + G_{\beta_p,F,1} K_{\beta_p,F,1})^{-1}$. Using the LMI optimization method, the controller $K_{\beta_p,F,1}$ is synthesized by minimizing the $\mathcal{H}_\infty$ norm of $T_{zw,\beta_p,F} = \left[ W_{S,\beta_p,F} S_{\beta_p,F,1} \quad W_{KS,\beta_p,F} K_{\beta_p,F,1} S_{\beta_p,F,1} \right]$, where
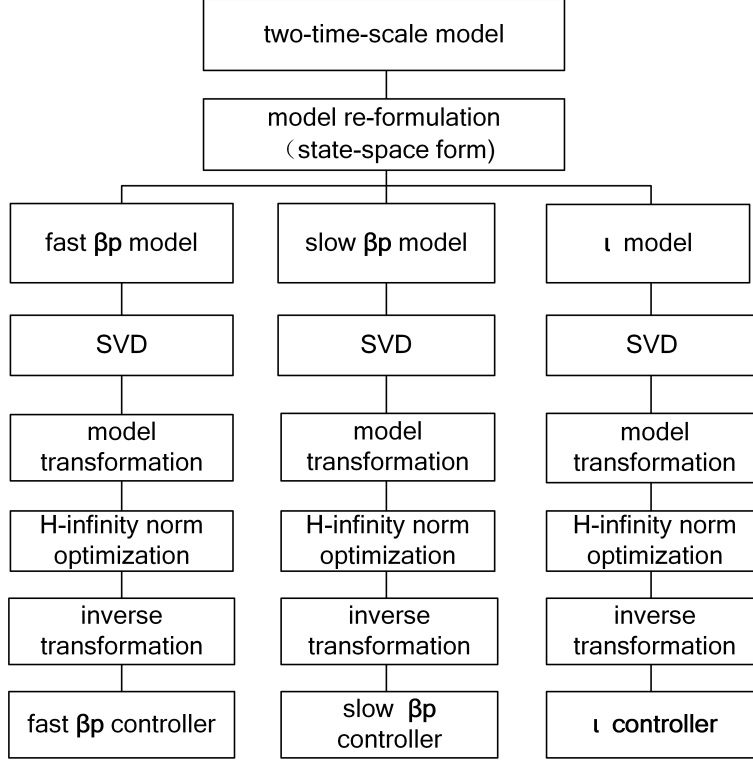
11

Figure 3: Schematic of the local controllers design

$W_{S,\beta_p,F}$ and $W_{KS,\beta_p,F}$ are two weighting functions. The fast $\beta_p$ controller is then obtained as $K_{\beta_F} = V_{1,1}\Sigma_{1,1}^{-1}K_{\beta_p,F,1}W_{1,1}$.

The slow $\beta_p$ controller is synthesized by shaping the mixed-sensitivity functions of the slow $\beta_p$ model. Similarly, an SVD technique is performed on the slow $\beta_p$ model at a cut-off frequency $\omega_{c,\beta_p,S} = 0$ rad/s to obtain the principal output and input control channels, expressed as $G_2 = W_2\Sigma_2 V_2^T$, where $G_2 = -C_{\beta_p,S}A_{\Psi}^{-1}B_{\Psi} + C_{\beta_p,S}$. For the slow $\beta_p$ controller, the lower closed-loop bandwidth is 0 rad/s, so $\omega_{c,\beta_p,S} = 0$ rad/s. Assume the first left and right singular vectors to be $W_{2,1}$ and $V_{2,1}$, which respectively represent the principal output and input control channel. The first singular value is $\Sigma_{2,1}$. Projecting $G_{\beta_p,S}$ onto the principal output and input control channels yields $G_{\beta_p,S,1} = W_{2,1}G_{\beta_p,S}V_{2,1}\Sigma_{2,1}^{-1}$. Assume that $K_{\beta_p,S,1}$ represents the transfer function of the controller for the plant $G_{\beta_p,S,1}$, we then obtain the sensitivity function $S_{\beta_p,S,1} = (I + G_{\beta_p,S,1}K_{\beta_p,S,1})^{-1}$. Using the LMI optimization method, the controller $K_{\beta_p,S,1}$ is synthesized by minimizing the $\mathcal{H}_\infty$

12

norm of $T_{zw,\beta_p,S} = \begin{bmatrix} W_{S,\beta_p,S}S_{\beta_p,S,1} & W_{KS,\beta_p,S}K_{\beta_p,S,1}S_{\beta_p,S,1} \end{bmatrix}$, where $W_{S,\beta_p,S}$ and $W_{KS,\beta_p,S}$ are two weighting functions. The slow $\beta_p$ controller is then obtained as $K_{\beta_S} = V_{2,1}\Sigma_{2,1}^{-1}K_{\beta_p,S,1}W_{2,1}$.

The $\iota$ controller is synthesized by shaping the mixed-sensitivity functions of the $\iota$ model. Similarly, an SVD technique is performed on the $\iota$ model at a cut-off frequency $\omega_{c,\iota} = 0$ rad/s to obtain the principal output and input control channels, expressed as $G_3 = W_3\Sigma_3 V_3^T$, where $G_3 = -C_\iota A_\Psi^{-1} B_\Psi + C_\iota$. For the $\iota$ controller, the lower closed-loop bandwidth is 0 rad/s, so $\omega_{c,\iota} = 0$ rad/s. Assume that the first $n$ left and right singular vectors to be $W_{3,n}$ and $V_{3,n}$, which represent the first $n$ principal output and input control channels. The first n singular values are $\Sigma_{3,n}$. In our case, $n$ is set at 1 because analysis shows that the second singular value is much smaller than the first one. Projecting $G_\iota$ onto the principal output and input control channels yields $G_{\iota,1} = W_{3,1}G_\iota V_{3,1}\Sigma_{3,1}^{-1}$. Assume that $K_{\iota,1}$ represents the transfer function of the controller for the plant $G_{\iota,1}$, we then obtain the sensitivity function $S_{\iota,1} = (I + G_{\iota,1}K_{\iota,1})^{-1}$. Using the LMI optimization method, the controller $K_{\iota,1}$ is synthesized by minimizing the $\mathcal{H}_\infty$ norm of $T_{zw,\iota} = \begin{bmatrix} W_{S,\iota}S_{\iota,1} & W_{KS,\iota}K_{\iota,1}S_{\iota,1} \end{bmatrix}$, where $W_{S,\iota}$ and $W_{KS,\iota}$ are two weighting functions. The $\iota$ controller is consequently obtained as $K_\iota = V_{3,1}\Sigma_{3,1}^{-1}K_{\iota,1}W_{3,1}$.

### 3.1.3. Combining the inputs for composite control

In order to achieve the simultaneous control of $\iota$ and $\beta_p$, the outputs of the $\iota$ and $\beta_p$ controllers should be combined to generate a set of actuated powers for the H&CD systems. Suppose that the output of the fast $\beta_p$ controller, of the slow $\beta_p$ controller and of the $\iota$ controller are $\vec{u}_{\beta_p,F}$, $\vec{u}_{\beta_p,S}$ and $\vec{u}_\iota$ respectively. Denoting $\vec{u}_{\beta_p} = \vec{u}_{\beta_p,F} + \vec{u}_{\beta_p,S}$ , the feedback controller output is expressed as:

$$\vec{u}_{FB} = (1 + \lambda_{\beta_p})\vec{u}_{\beta_p} + (1 + \lambda_\iota)\vec{u}_\iota \tag{15}$$

where

$$\lambda_{\beta_p} = \frac{\left(\frac{\vec{u}_\iota \cdot \vec{u}_{\beta_p}}{\|\vec{u}_\iota\|\|\vec{u}_{\beta_p}\|}\right)^2 - \frac{\vec{u}_\iota \cdot \vec{u}_{\beta_p}}{\|\vec{u}_{\beta_p}\|^2}}{1 - \left(\frac{\vec{u}_\iota \cdot \vec{u}_{\beta_p}}{\|\vec{u}_\iota\|\|\vec{u}_{\beta_p}\|}\right)^2}, \lambda_\iota = \frac{\left(\frac{\vec{u}_{\beta_p} \cdot \vec{u}_\iota}{\|\vec{u}_{\beta_p}\|\|\vec{u}_\iota\|}\right)^2 - \frac{\vec{u}_{\beta_p} \cdot \vec{u}_\iota}{\|\vec{u}_\iota\|^2}}{1 - \left(\frac{\vec{u}_{\beta_p} \cdot \vec{u}_\iota}{\|\vec{u}_{\beta_p}\|\|\vec{u}_\iota\|}\right)^2}$$

Here, $\lambda_{\beta_p}$ and $\lambda_\iota$ are the decoupling coefficients which ensure that the projection of $\vec{u}_{FB}$ onto the direction of $\vec{u}_{\beta_p}$ is the magnitude of $\vec{u}_{\beta_p}$ and meanwhile, the projection of $\vec{u}_{FB}$ onto the direction of $\vec{u}_\iota$ is the magnitude of $\vec{u}_\iota$. Details of the computation are given in the Appendix A. We consider the

Table 1: Weighting functions for $S/KS$

| Option | $W_S$ | $W_{KS}$ |
|---|---|---|
| I | $\frac{\frac{s}{M}+\omega_B}{s+\omega_B A}$ | $1$ |
| II | $\frac{(\frac{s}{\sqrt{M_p}}+\omega_p)^2}{(s+\omega_p\sqrt{A_p})^2}$ | $\frac{(\frac{s}{\sqrt{M_u}}+\omega_u)^2}{(s+\omega_u\sqrt{A_u})^2}$ |

constant feedforward $\vec{u}_{FF}$ to be the steady-state powers for the plasma equilibrium around which the model is linearized. The total actuated powers for the H&CD systems are then obtained as $U = \vec{u}_{FB} + \vec{u}_{FF}$.

### 3.1.4. Remarks on the weighting functions

In this work, two options of the weighting functions $W_S/W_{KS}$ [32, 9] to shape the $\mathcal{H}_\infty$ norm of the mixed sensitivity function $S/KS$ are attempted, as listed in Table 1.

In option I, the sensitivity function $S$ is shaped by the weighting function $W_S = \frac{\frac{s}{M}+\omega_B}{s+\omega_B A}$. We select $A << 1$ to ensure the approximate integral action with $S(0) \approx 0$ such that the tracking error can be made small and the output disturbance can be attenuated. We keep $M$ fixed at 2 for all the controlled outputs. The desired closed-loop bandwidth $\omega_B$ are tuned by trials and errors, which is directly related to the transient performance. A large value of $\omega_B$ yields a faster response for the controlled output, but it may result in larger overshoots.

In option II, the mixed-sensitivity functions $S$ and $KS$ are respectively shaped by $\frac{(\frac{s}{\sqrt{M_p}}+\omega_p)^2}{(s+\omega_p\sqrt{A_p})^2}$ and $\frac{(\frac{s}{\sqrt{M_u}}+\omega_u)^2}{(s+\omega_u\sqrt{A_u})^2}$, implying more tuning parameters. The parameters $M_p$ and $M_u$ are associated with the high frequency behaviour, which are fixed at 2. The parameters $A_p$ and $A_u$ are related to the low frequency behaviour and we select them to be small for good tracking and disturbance rejection. The parameters $\omega_p$ and $\omega_u$ determine the closed-loop control bandwidth [13], which are tuned by trials and errors.

### 3.2. Control implementation

### 3.2.1. Setpoints selection

The setpoints selection is essential for the situation where the number of outputs is larger than that of inputs, because if the setpoints are specified out of the attractive control region they should never be achieved even with the maximum/minimum allowed actuations. In this study, the $\iota$ and

14

$\beta_p$ sepoints are determined semi-empirically by nonlinear closed-loop METIS simulations such that all the setpoints are located in the attractive control region.

### 3.2.2. Control discretization and model reduction

Using the $\mathcal{H}_\infty$ norm optimization approach we consequently derive a set of continuous dynamical controllers with different orders.The real-time application to plasma control requires the discretisation of these controllers. Accounting for the constraints of the equilibrium reconstruction and energy confinement time on EAST, we discretize the controller with the sampling time $T_s = 20$ ms.

For simplicity, one can further perform model reduction on these discrete controllers to remove insignificant controller dynamics and obtain their minimal realizations [32]. After model reduction, the order of the fast $\beta_p$ controller remains at 2 by using the weighting functions in option I. The initial order of the fast $\beta_p$ controller (2) is equal to the sum of the order of the fast $\beta_p$ model (1) and of the weighting functions (1). The slow $\beta_p$ controller order substantially decreases for example by using the weighting functions in option II, from 14 to 8. The initial order of the slow $\beta_p$ controller (14) is the sum of the order of the slow $\beta_p$ model (10) and of the weighting functions $(2 + 2)$. The order of $\iota$ controller drops from 14 to 5. The initial order of the $\iota$ controller (14) is the sum of the order of the $\iota$ model (10) and of the weighting functions $(2 + 2)$.

### 3.2.3. Feedforward and control initialization

The control initialization is important for good control performance, because if it is not well configured, the actuations are probably saturated which may cause large overshoots, even plasma disruptions. To avoid the possibilties of potential plasma disruptions arising from improper control initialization, a feedforward in terms of discrete low-pass filters for $\iota$ and $\beta_p$ is designed. The characteristic time for the $\iota$ and $\beta_p$ pre-filters are respectively of the order of the resistive diffusion time $\tau_{\mathrm{mag}} = 0.4$ s and the energy confinement time $\tau_{\mathrm{kin}} = 0.04$ s. The feedforward trajectories are

15

then obtained as follows in the discrete state space form:

$$
\begin{bmatrix} x_\iota[k+1] \\ x_{\beta_p}[k+1] \end{bmatrix} = \begin{bmatrix} A_{f,\iota} & 0 \\ 0 & A_{f,\beta_p} \end{bmatrix} \begin{bmatrix} x_\iota[k] \\ x_{\beta_p}[k] \end{bmatrix} +
$$
$$
\begin{bmatrix} B_{f,\iota} & 0 \\ 0 & B_{f,\beta_p} \end{bmatrix} \begin{bmatrix} \iota_{\mathrm{ref}}[k] \\ \beta_{\mathrm{p,ref}}[k] \end{bmatrix} \tag{16}
$$
$$
\begin{bmatrix} \iota_m[k] \\ \beta_{p,m}[k] \end{bmatrix} = \begin{bmatrix} C_{f,\iota} & 0 \\ 0 & C_{f,\beta_p} \end{bmatrix} \begin{bmatrix} x_\iota[k] \\ x_{\beta_p}[k] \end{bmatrix}
$$

where $\iota_{\mathrm{ref}}[k]$ and $\beta_{\mathrm{p,ref}}[k]$ are respectively the setpoints selected in section (3.2.1) for $\iota$ and $\beta_p$ at time k, $x_\iota[k]$ and $x_{\beta_p}[k]$ the filter states at time k, while $\iota_m[k]$ and $\beta_{p,m}[k]$ respectively denote the $\iota$ and $\beta_p$ reference trajectories at time k for the feedback controller to track.

To avoid undesirable bump and power saturations due to control switching [34][32], the initial states of the $\iota$ and $\beta_p$ filters are then computed as

$$
\begin{bmatrix} x_\iota[0] \\ x_{\beta_p}[0] \end{bmatrix} = \begin{bmatrix} C_{f,\iota} & 0 \\ 0 & C_{f,\beta_p} \end{bmatrix}^{-1} \begin{bmatrix} \iota_{\mathrm{mea}}[0] \\ \beta_{\mathrm{p,mea}}[0] \end{bmatrix} \tag{17}
$$

Here we assume that k = 0 represents the starting time when the feedback controller is switched on. $\iota_{\mathrm{mea}}[0]$ and $\beta_{\mathrm{p,mea}}[0]$ indicate the initial measured/estimated $\iota$ and $\beta_p$ respectively, which are equal to their corresponding initial setpoints $\iota_{\mathrm{ref}}[0]$ and $\beta_{\mathrm{p,ref}}[0]$ .

### 3.2.4. Actuator dynamics

In order to mimick the experimental conditions for auxiliary H&CD power actuators on EAST, actuation dynamics are considered to evaluate the performance and robustness of the feedback control algorithm. The actuation dynamics for the ICRH and LHCD are modelled separately as a first-order time-delay transfer function:

$$
G_i(s) = \frac{k_i}{\tau_i s + 1} e^{-\theta_i s}, i \in \{\mathrm{ICRH, LHCD}\} \tag{18}
$$

where i is an indicator for power actuators, $k_i$ the i-th steady-state gain which is fixed at 1, $\tau_i$ the i-th characteristic time, $\theta_i$ the i-th time delay and $G_i(s)$ the transfer function for the i-th power actuator. A saturation module that accounts for both the magnitude and rate limits of ICRH and LHCD is considered. Table 2 lists the related parameter values, where $\mathrm{S}_m$ and $\mathrm{S}_r$ respectively denote the magnitude and rate limits allowed by the actuators.

Table 2: ICRH and LHCD power actuator model paramters

| Actuators | $\tau_i$ [ms] | $\theta_i$ [ms] | $S_m$ [MW] | $S_r$ [MW· s $^{-1}$] |
|---|---|---|---|---|
| ICRH | 1 | [0, 60] | [0, 1.5] | [-8, 8] |
| LHCD | 1 | [0, 60] | [0, 3] | [-8, 8] |

*3.2.5. Control conditioning and anti-windup compensation*

Since there are a series of dynamics in the actuated power systems, the actual delivered powers are never totally equal to the control commands requested by the controller at each time slice. However, the controller cannot automatically identify whether the commands are followed or not unless an extra closed loop is involved. In some cases, for instance, due to power saturations and time delays, the states of the controller may wind up because the plant does not respond accordingly, so that the behaviour of the system will deteriorate dramatically. To handle this problem, an anti-windup compensator is designed to keep the controller well-behaved and avoid undesirable oscillations when saturations and moderate time delays are present, which is expressed in the discrete state-space form:

$$
\begin{bmatrix} x_{aw}[k+1] \\ y_{aw,d}[k] \end{bmatrix} = \begin{cases} \begin{bmatrix} A_{aw} & B_{aw} \\ C_{aw} & D_{aw} \end{bmatrix} \begin{bmatrix} x_{aw}[k] \\ \delta u[k] \end{bmatrix} & ,\text{if} \quad \delta u[k] \neq 0 \\ \begin{bmatrix} A_{exp} \\ C_{exp} \end{bmatrix} x_{aw}[k] & ,\text{if} \quad \delta u[k] = 0 \end{cases}
\tag{19}
$$

Here $\delta u = u_a[k] - u_c[k]$, $u_a[k]$ denotes the measurements of the actuated powers and $u_c[k]$ denotes the control outputs of the controller. The system matrices $(A_{aw}, B_{aw}, C_{aw}, D_{aw})$ of the anti-windup compensator are chosen identical to the discrete form of the system matrices in the two-time-scale plasma model. $(A_{exp}, C_{exp})$ is a discrete state-space realization of the asymptotically stable equation $\dot{x}_{aw}(t) = \lambda x_{aw}(t)$, and $\lambda$ is set to be -50. $y_{aw,d}[k]$ is the modified reference arising from the actuation dynamics to be added to the reference trajectories for controller states conditioning in real-time. This conditioning technique can be combined with the fast and slow $\beta_p$ controller to cope with up to 60 ms of time delays plus power saturations, which will be demonstrated in Section 4.2.

17

*3.2.6. Real-time capability*

Testing on a computer with Intel(R) Xeon (R) CPU X5660@2.8GHz processors shows that the average computational time for one control cycle is 40.6 $\mu$s (less than the sampling time 20 ms). Considering that the current implementation of the control algorithms is based on the MAT-LAB/Simulink framework, the computation time for each control cycle should be further reduced when the algorithm is realized by the C/C++ code and implemented into the EAST plasma control system (PCS) using the embedded MATLAB coder (EMC) toolbox. Therefore, we conclude that this algorithm meets the real-time constraints.

*3.2.7. Performance Indexes*

The feedback control performance is evaluated based on a set of indexes that can be used to represent the control performance in different aspects.

The first index is the rise time, which is defined as the total time required for the response to rise/fall from 10 % (90 %) to 90 % (10 %) of its regulation height in a specific time window. Specifically, we assume that there are N time windows for the regulation of $\iota$ and $\beta_p$ in a controlled scenario, and the starting time for the $\iota$ and $\beta_p$ setpoint transition remain the same. In a given time window n, the rise time of $\iota$ at $x = 0, 0.1, 0.2, ..., 0.9$ ($t_{r,\iota}(n,x)$) and $\beta_p$ ($t_{r,\beta_p}(n)$) read as:

$$
\begin{aligned}
t_{r,\iota}(n,x) =& t(\iota_a^1(n,x)) - t(\iota_a^0(n,x)) \\
t_{r,\beta_p}(n) =& t(\beta_{p,a}^1(n)) - t(\beta_{p,a}^0(n))
\end{aligned}
\tag{20}
$$

where

$$
\begin{bmatrix} \iota_a^1(n,x) & \beta_{p,a}^1(n) \\ \iota_a^0(n,x) & \beta_{p,a}^0(n) \end{bmatrix} = \begin{bmatrix} 0.1 & 0.9 \\ 0.9 & 0.1 \end{bmatrix} \begin{bmatrix} \iota_0(n,x) & \beta_{p,0}(n) \\ \iota_1(n,x) & \beta_{p,1}(n) \end{bmatrix}
$$

$$
n = 1, 2, .., N, \quad x = 0, 0.1, 0.2, ..., 0.9
$$

Here, $\iota_0(n,x)$ and $\beta_{p,0}(n)$ are the starting setpoints of $\iota(x)$ and $\beta_p$ in the time window n respectively, while $\iota_1(n,x)$ and $\beta_{p,1}(n)$ indicate the final setpoints. Likewise, $\iota_a^0(n,x)$ and $\beta_{p,a}^0(n)$ are the estimated/measured values at the 10 % of the regulation heights in a given time window n, while $\iota_a^1(n,x)$ and $\beta_{p,a}^1(n)$ are those at the 90 % of the regulation heights.

Once the rise times for $\iota$ and $\beta_p$ in a time window are obtained, we can then calculate the averaged values. For $\iota$, averaging the rise time $t_{r,\iota}(n,x)$ on n can represent the averaged rise time at each point over all the time windows, i.e. $\langle t_{r,\iota}(n,x) \rangle_n$, meanwhile averaging $t_{r,\iota}(n,x)$ on x can

express the integrated rise time of $\iota$ points in different time windows, i.e. $\langle t_{r,\iota}(n,x)\rangle_x$. $\langle t_{r,\iota}\rangle$ and $\langle t_{r,\beta_p}\rangle$ are two scalars which show the comprehensive response time for $\iota$ and $\beta_p$ respectively. Note that $W(x)$ is the normalized weighting matrix which represents the importance of each point.

$$\langle t_{r,\iota}\rangle = \frac{1}{10N}\sum_{x=0}^{0.9}\sum_{n=1}^{N}W(x)t_{r,\iota}(n,x)$$

$$\langle t_{r,\beta_p}\rangle = \frac{1}{N}\sum_{n=1}^{N}t_{r,\beta_p}(n)$$

$$\langle t_{r,\iota}(n,x)\rangle_n = \frac{1}{N}\sum_{1}^{N}t_{r,\iota}(n,x)$$

$$\langle t_{r,\iota}(n,x)\rangle_x = \frac{1}{10}\sum_{x=0}^{0.9}W(x)t_{r,\iota}(n,x)$$

The second performance index is the overshoot, which is defined as the maximum amount a system overshoots its final value divided by its final value, often expressed in percentage. In tokamak plasma operation, large overshoots of $\iota$ and $\beta_p$ can result in undesirable MHD and kinetic instabilities, thus it is good to quantify this index to reflect the control performance. For our problem, since $\iota$ and $\beta_p$ are not the same kind of physical quantities, we define $l_{os,\iota}(n,x)$ and $l_{os,\beta_p}(n)$ respectively as the overshoot of $\iota(x)$ and $\beta_p$ at a given time window n.

$$l_{os,\iota}(n,x) = \frac{\iota_{max}(n,x) - \iota_{ss}(n,x)}{\iota_{ss}(n,x)} \times 100\%$$

$$l_{os,\beta_p}(n) = \frac{\beta_{p,max}(n) - \beta_{p,ss}(n)}{\beta_{p,ss}(n)} \times 100\% \tag{21}$$

$$n = 1, 2, .., N, \quad x = 0, 0.1, 0.2, ..., 0.9$$

where $\iota_{max}(n,x)$ and $\beta_{p,max}(n)$ are respectively the maximum values exceeding their corresponding steady state values $\iota_{ss}(n,x)$ and $\beta_{p,ss}(n)$.

With the similar technique, we can derive two scalars, i.e. $\langle l_{os,\iota}\rangle$ and $\langle l_{os,\beta_p}\rangle$ for the comprehensive evaluation of $\iota$ and $\beta_p$ overshoots in the whole controlled scenario. Two partial averaged values $\langle l_{os,\iota}(n,x)\rangle_n$ and $\langle l_{os,\iota}(n,x)\rangle_x$ represent the overshoots of $\iota$ in two different aspects. The weighting

19

matrix $W(x)$ is the same as the one for the rise time calculation.

$$\langle l_{os,\iota} \rangle = \frac{1}{10N} \sum_{x=0}^{0.9} W(x) \sum_{n=1}^{N} l_{os,\iota}(n,x)$$

$$\langle l_{os,\beta_p} \rangle = \frac{1}{N} \sum_{n=1}^{N} l_{os,\beta_p}(n)$$

$$\langle l_{os,\iota}(n,x) \rangle_n = \frac{1}{N} \sum_{n=1}^{N} l_{os,\iota}(n,x)$$

$$\langle l_{os,\iota}(n,x) \rangle_x = \frac{1}{10} \sum_{x=0}^{0.9} W(x) l_{os,\iota}(n,x)$$

The third performance index is the relative error index, which represents the relative error of the controlled output against its setpoint. For our problem, $J_\iota[k]$ and $J_{\beta_p}[k]$ are two time-variant relative error indexes for $\iota$ and $\beta_p$ respectively. These two indexes are defined as:

$$J_\iota[k] = \frac{\delta \iota^T[k] Q \delta \iota[k]}{\iota_r^T[k] Q \iota_r[k]}, \quad \delta \iota[k] = \iota[k] - \iota_r[k]$$

$$J_{\beta_p}[k] = \frac{\delta \beta_p^T[k] \delta \beta_p[k]}{\beta_{p,r}^T[k] \beta_{p,r}[k]}, \quad \delta \beta_p[k] = \beta_p[k] - \beta_{p,r}[k]$$

(22)

where $Q$ is the weighting matrix for $\iota$, $\delta \iota$ ($\delta \beta_p$) is the error between the estimation $\iota[k]$ ($\beta_p[k]$) and the setpoint $\iota_r[k]$ ($\beta_{p,r}[k]$). Averaging them can as well attain the overall relative error indexes for $\iota$, i.e. $\langle J_\iota \rangle$ and $\beta_p$, i.e. $\langle J_{\beta_p} \rangle$, where K is the number of samplings in the whole controlled process.

$$\langle J_\iota \rangle = \frac{1}{K} \sum_{k=1}^{K} J_\iota[k], \quad \langle J_{\beta_p} \rangle = \frac{1}{K} \sum_{k=1}^{K} J_{\beta_p}[k]$$

We do not combine them by adding these two scalars for a comprehensive representation of the control performance because we note that they may evolve in different orders, and adding them may neglect important information about control performance.

## 4. Simulation Results

In order to evaluate the control scheme proposed in the previous section, closed-loop simulations were carried out by coupling the controller with the METIS code, which is a non-linear plasma simulator.

20

The two-time-scale model is identified from 20 different METIS open loop simulations with random power modulations: the details of the system identification methodology can be found in [22, 26, 27]. The reference scenario around which the model is identified is a steady state, fully non-inductive single-null H-mode discharge in the EAST tokamak, i.e. Shot #62946, with the toroidal magnetic field $B_T = 2.5$ T, the central electron density $n_{e0} \approx 3.5 \times 10^{19}$ m$^{-3}$ and plasma current $I_p = 0.42$ MA. The discharge was obtained using LHCD (0.6 MW at 2.45 GHz and 2 MW at 4.6 GHz), 0.32 MW of ICRH at 33 MHz and 0.3 MW of ECRH at 140 GHz. The transition to H-mode occurred at 3.1 s with an H-mode enhancement factor H$_{98}(y,2) \sim 1.1$. The q profile exhibited a small negative shear in the plasma core, with minimum q around 1.5 and $q_0 \sim 2$ on axis. The plasma profiles were retrieved from the EFIT magnetic equilibrium reconstructions available in real-time using magnetic and kinetic measurements, for instance, interfero-polarimetry data from the POINT diagnostics[35, 36, 37].

The initialization of the METIS code is preset to be consistent with Shot #62946 at 3.1 s, including plasma current, shape, magnetic fluxes, kinetic profiles and actuated powers. The plasma transport model is described in detail in [28] and was chosen consistent with the standard ITER-EIV H-mode scaling law [38]. With this scaling law, an H-factor of 0.99 was used in METIS simulations to fit the measured plasma energy content. This H-factor can be varied in some simulations to study the effect of model perturbations. Some other fitting parameters were chosen in order to fit the temperature profiles measured in Shot #62946 and then fixed for all simulations. The LHCD model is also described in [28]. The lower hybrid power deposition profile is based on a probabilistic ad-hoc formulation which takes into account the limits of the wave propagation domain in space and parallel wave-index and the Landau absorption criterion as a function of local plasma temperature. With the chosen parameters, the LHCD was generally deposited off-axis, which could lead to reverse magnetic shear at high power, and to the formation of electron internal transport barriers in some cases. Plasma parameters such as plasma current, geometry, densities and effective charge numbers are assumed to be regulated by dedicated controllers. The sampling time is fixed to 20 ms. The LHCD power at 2.45 GHz and the ECRH power at 140 GHz are not considered as control actuators. They are always at their reference values in every simulation, 0.6 MW and 0.3 MW respectively, and since METIS allows for only one lower hybrid system, they are combined into a single heating system providing 0.9 MW with given power and current deposition profiles into the plasma at constant plasma current and density. The control actuators

are the LHCD power at 4.6 GHz and the ICRH power at 33 MHz and their feedforward components are constant at 2 MW and 0.32 MW, respectively, as in the reference discharge. The time constants for $\beta_p$ and $\iota$ prefilters are respectively 0.04 s and 0.4 s, whose initial states are respectively 1.0282 ($\beta_{p,0}$) and [0.9200, 0.9032, 0.9745, 0.9901, 0.7892, 0.6195, 0.4602, 0.3383, 0.2496, 0.1866] ($\iota_{i,0}, i = 0, 0.1, 0.2, ..., 0.9$) corresponding to the counterparts at 3.1 s in Shot #62946. The time constant and initial state for the low-pass filter in the feedback component are 1 s and 0 respectively. The actuated powers are the 4.6 GHz LHCD spreading between 0 and 3 MW and the 33 MHz ICRH from 0 to 1.5 MW.

### 4.1. Tracking of q-profile and $\beta_p$

#### 4.1.1. Separate control of $\beta_p$ and the core $\iota$ profile

The simplest control evaluation case is the nominal control of $\beta_p$, with the safety factor control relaxed as shown in Fig. 4. There are totally 6 setpoints which are required to be achieved, sequentially 1.5, 2, 3, 1.9, 2.3 and 2.8. It is obvious that the combination of fast $\beta_p$ and slow $\beta_p$ controllers is able to track $\beta_p$ with good control performance, e.g. the averaged rise time $\langle t_{r,\beta_p} \rangle$ at 132 ms, very small overshoots ($\langle l_{os,\beta_p} \rangle = 3.2$ %) and negligible steady-state errors under the condition that the powers of ICRH and LHCD are not saturated. In each control phase, the averaged relative error for $\beta_p$, i.e. $\langle J_{\beta_p} \rangle$, initialy increases due to the sudden change of its regulation point, and then decreases substantially to around $10^{-7}$. It must be noted here that the sampling time was set to 0.02 s for the control simulations, i.e. for both the controller inputs/outputs and the METIS evolution. This allowed extensive closed-loop simulations to be performed in a reasonable time despite the complexity of the METIS code, and also provided realistic simulations of the closed-loop experiments on EAST, in which the sampling time has to match the requirements of the real-time magnetic reconstruction. This sampling time is adequate for the slow $\beta_p$ controller (the characteristic time of the slow model is $\tau_{mag} = 0.4$s), but discrepencies between the (ideal) continuous dynamics and the discrete ones due to sampling may influence the fast control of $\beta_p$ (the characteristic time of the fast model is $\tau_{kin} = 0.04$s). Since the rise time $\langle t_{r,\beta_p} \rangle$ is around six times the sampling interval and 3.5 $\tau_E$, this influence appears to be insignificant. Concerning the evolution of the $\iota$ values at different radii, we note that the plasma temperature increases when the ICRH power and $\beta_p$ increase, which makes the LHCD deposition more off-axis and also drives more bootstrap current, thus leading to the increase of the core safety factor profile.
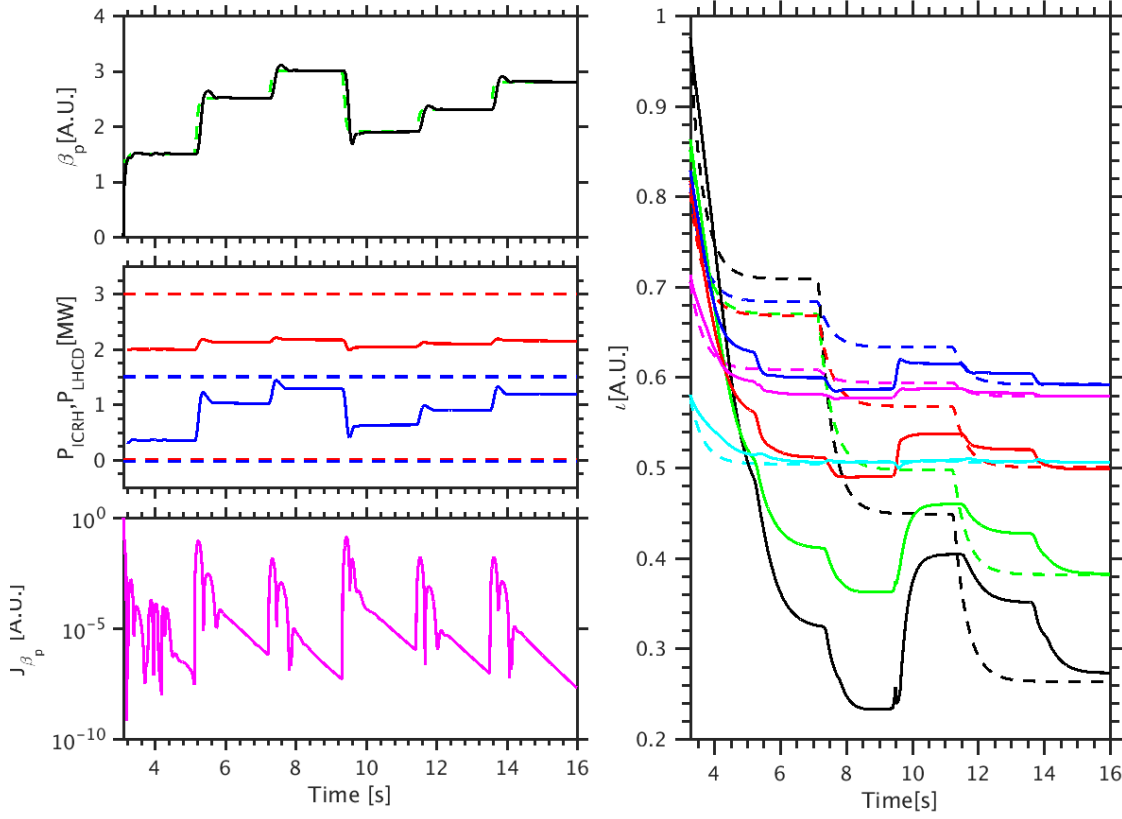
22

Figure 4: Tracking $\beta_p$. Left-top panel: time traces of $\beta_p$ setpoints (green dashed) and evolutions (black) with $\beta_p$ feedback control. Left-middle panel: time traces of actuated powers $P_{ICRH}$ (blue) and $P_{LHCD}$ (red), as well as the ICRH (blue dashed) and LHCD (red dashed) power limits. Left-bottom panel: time traces of the relative error index for $\beta_p$. Right panel: time traces of $\iota$ setpoints (dashed) and evolutions (solid) at x = 0 (black), 0.1 (green), 0.2 (red), 0.3 (blue), 0.4 (magenta), 0.5 (cyan) with $\iota$ control relaxed.

The second case is the nominal control of $\iota$ values at normalized radius x = 0, 0.1, 0.2, ..., 0.5 with the $\beta_p$ feedback control relaxed. Three sets of setpoints were prescribed, with the first setpoint globally positive magnetic shear, the second one being weakly negatively sheared in the plasma core, and the third being strongly centrally negatively sheared. As shown in Fig. 5, the setpoints are achieved with the averaged rise time $\langle t_{r,\iota} \rangle = 607$ ms and the averaged overshoots $\langle l_{os,\beta_p} \rangle = 1.4$ %. In each control phase, the averaged relative error for $\iota$, i.e. $\langle J_\iota \rangle$, initialy increases due to its limited control bandwidth, and then decreases exponentially to around $10^{-6}$. Since the plasma pressure is

23

not actively controlled, in other words, the fast and slow $\beta_p$ controllers are not switched on, the $\beta_p$ value remains at around 1.5 due to very small variations of the ICRH power. It indicates that, as expected, the LHCD system is more suitable for $\iota$ control than for $\beta_p$ control, while the ICRH system is just in reverse. In addition, small variations of $\beta_p$ indicate that the control of $\iota$ points in the plasma core via LHCD does not obviously impact the value of plasma pressure.
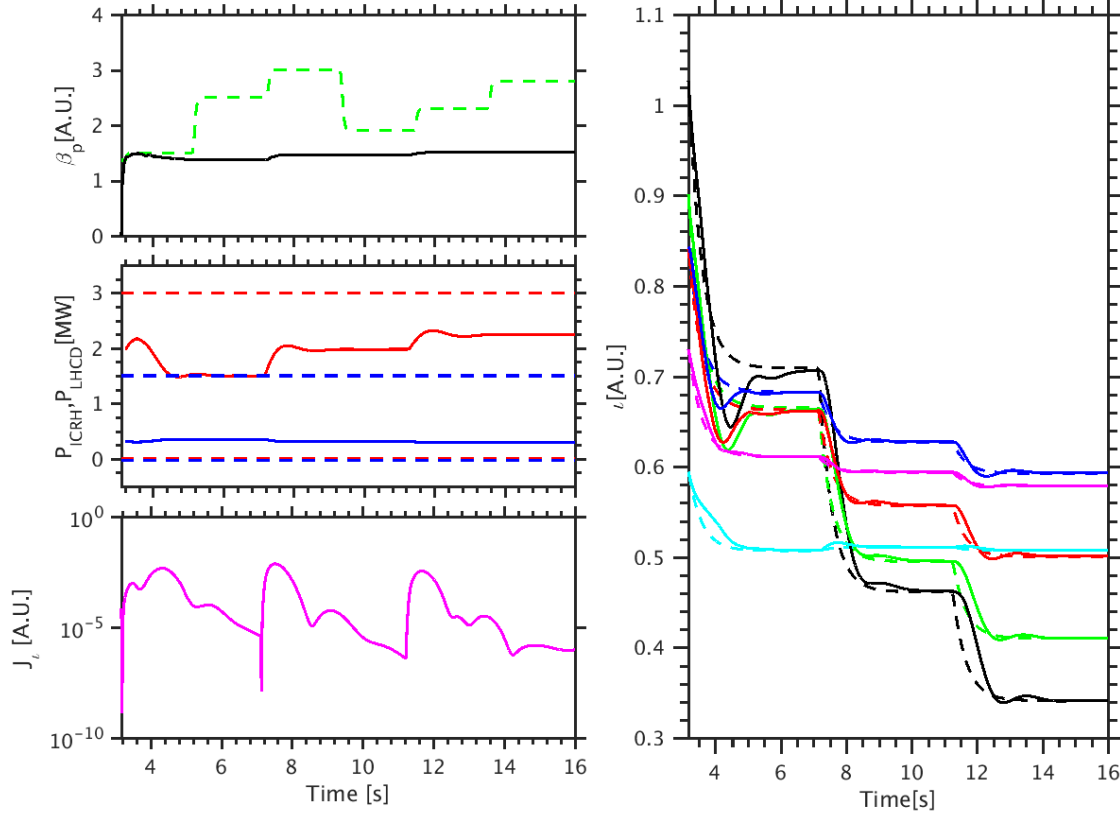


Figure 5: Tracking $\iota$ points at 0, 0.1, 0.2, ...,0.4. Left-top panel: time traces of $\beta_p$ setpoints (green dashed) and evolutions (black) with $\beta_p$ control relaxed. Left-middle panel: time traces of actuated powers $P_{ICRH}$ (blue) and $P_{LHCD}$ (red), as well as the ICRH (blue dashed) and LHCD (red dashed) power limits. Left-bottom panel: time traces of the averaged relative error index for $\iota$. Right panel: time traces of $\iota$ setpoints (dashed) and evolutions (solid) at x = 0 (black), 0.1 (green), 0.2 (red), 0.3 (blue), 0.4 (magenta), 0.5 (cyan) with $\iota$ feedback control.

24

### 4.1.2. Simultaneous control of $\beta_p$ and the core $\iota$ profile

The nominal control of both $\iota$ and $\beta_p$ is shown in Fig. 6. Three $\beta_p$ setpoints, namely 2, 2.5 and 3, are prescribed, i.e. 2 in the time interval [3.1, 7.1] s, 2.5 in [7.2, 11.2] s and 3 in [11.3, 15.6] s. Likewise, three groups of setpoints for $\iota$ at 0, 0.1,..., 0.4 are specified, i.e. positive central magnetic shear between 3.1 s and 7.1 s, weakly central negative shear from 7.2 s to 11.2 s and strongly central negative shear in [11.3, 15.6] s. Clearly, all the targets are achieved using only the limited LHCD and ICRH powers, with the averaged rise time vector $(\langle t_{r,\beta_p} \rangle, \langle t_{r,\iota} \rangle)$ at (0.113, 1.11) s, the averaged overshoot vector $(\langle l_{os,\beta_p} \rangle, \langle l_{os,\iota} \rangle)$ at (1.44, 3.47) %. In each regulation window, $J_\iota$ evolves from $10^{-3}$ to $10^{-5}$ and $J_{\beta_p}$ decreases from $10^{-2}$ to approximately $10^{-9}$.

The corresponding evolutions of q-profile, the bootstrap current profile, electron and ion temperature profiles are depicted in Fig. 7. With the decrease of the central magnetic shear and the $\beta_p$ increase, the bootstrap current was increased due to the increase of electron temperatures and their gradients and the LH-driven current was increased as well via actuating more LHCD power. An internal transport barrier was formed on the electron channel as one can notice a strong increase of $T_e$ and $J_{\text{boot}}$ in the center. However, the increase of electron temperatures implies the reduction of the electron-ion collision frequency (proportionally to $T_e^{-1.5}$), hence the ions could not be heated by electrons. Taking the ion radiation and power loss into account, the ions temperature dropped slightly.

The EAST tokamak is a superconducting tokamak which is suitable for the long-pulse steady-state plasma operation. The second case involves the simulatenous control of $\beta_p$ and $\iota$ in H-mode steady state operational scenarios. In order to design appropriate $\iota$ and $\beta_p$ setpoints for H-mode steady-state plasma control, we perform trial simulations by regulating one set of $\iota$ values via the proposed $\iota$ controller and tracking $\beta_p$ to different levels via the proposed $\beta_p$ controller. The pair of $\iota$ and $\beta_p$ values associated with zero surface loop voltage are selected as setpoints. Note that $U_{loop}$ is not an actuator, and the condition of the zero loop voltage with the constant total plasma current is satified by appropriately coordinating the values of $\iota$ and $\beta_p$. With the procedure, three pairs of setpoints for $\iota$ and $\beta_p$ are therefore designed. The tracking of these designed setpoints using the proposed control scheme is then performed with the results shown in Fig. 8. In each regulation window, the setpoints are reached with the averaged rise time vector $(\langle t_{r,\beta_p} \rangle, \langle t_{r,\iota} \rangle)$ at (0.146, 1.34) s, the averaged overshoot vector at $(\langle l_{os,\beta_p} \rangle, \langle l_{os,\iota} \rangle)$ at (2.13, 3.86) %, small steady state errors, and meanwhile, with the loop voltage approaching zero.
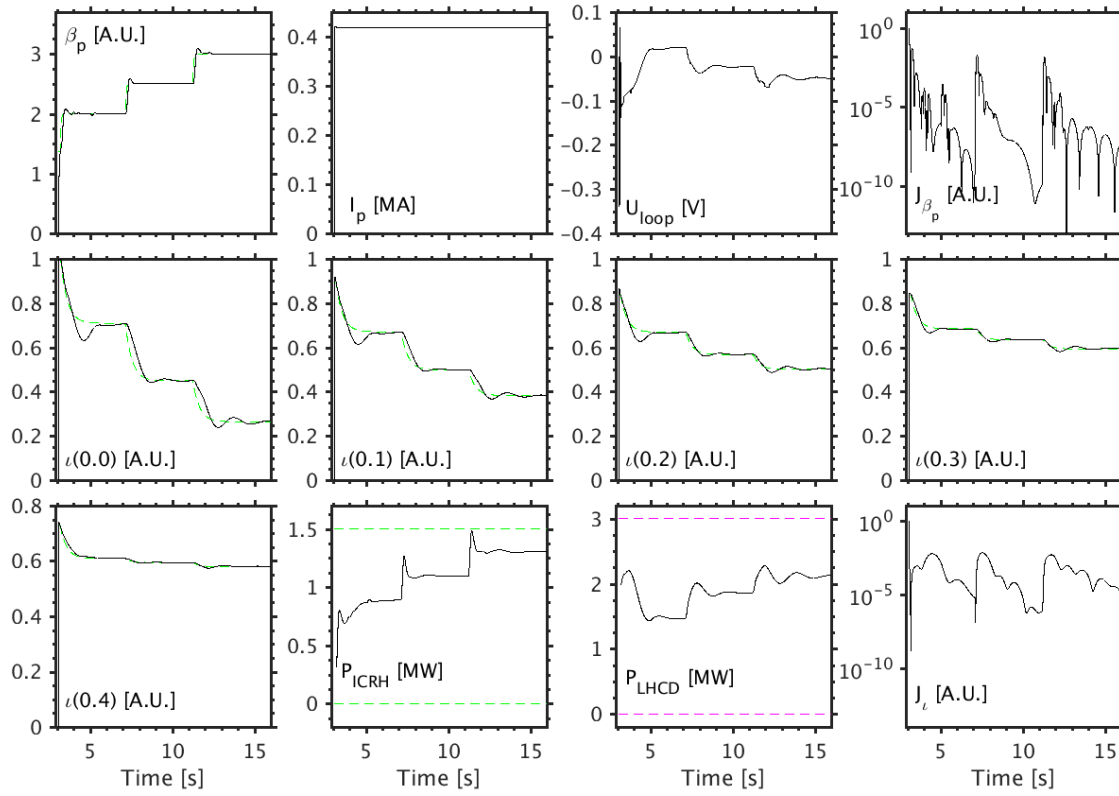
Figure 6: Tracking $\iota$ points at 0, 0.1, 0.2, ..., 0.4 and $\beta_p$ simultaneously. Top panels from left to right: time traces of plasma poloidal pressure $\beta_p$, plasma current $I_p$, the loop voltage $U_{loop}$, the averaged relative error for $\beta_p$, $\langle J_{\beta_p} \rangle$. Middle panels from left to right: time traces of the $\iota$ septpoints (green dashed) and evolutions (black solid) at x = 0, 0.1, 0.2, 0.3. Bottom panels: time traces of the $\iota$ setpoints (green dashed) and evolutions (black solid) at x = 0.4, the actuated ICRH power $P_{ICRH}$ (black solid) associated with its power limits (green dashed), the ICRH power $P_{LHCD}$ (black solid) associated with its power limits (magenta dashed), and the averaged relative error for $\iota$, $\langle J_\iota \rangle$.

More interesting physical results are illustrated in Fig. 9. It seems that the increase of the absolute value of central magnetic shear combined with the $\beta_p$ decrease can ensure the sum of bootstrap current and LH driven current approximately kept at a level so that the ohmic current would not play a role. With the decrease of the ICRH power, $\beta_p$ drops from 2.8 to 2.2, associated with the global reduction of the electron temperature. The decrease of electron temperatures results in the growth of the collision frequency between electrons and ions, thus the ion temperatures globally increased via acquiring the energy from electrons. The two obvious bulbs for the
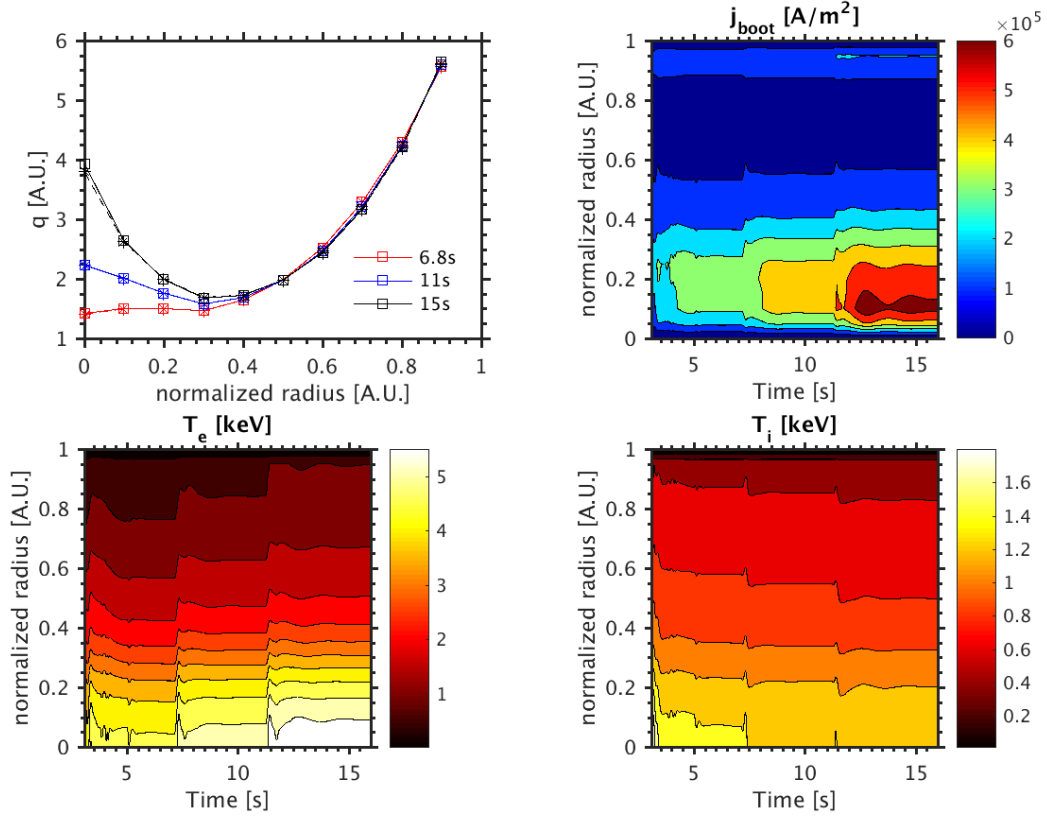
26

Figure 7: Simulation of a hybrid scenario. Left-top panel: typical q-profile setpoints (asterisk and dashed) and evolutions (square and solid) at 6.8 s (red), 11 s (blue) and 15 s (black). Right-top panel: contour plot of the bootstrap current $j_{boot}$ evolution. Left-bottom panel: contour plot of the electron temperature profile $T_e$ evolution. Right-bottom panel: contour plot of the ion temperature profile $T_i$ evolution.

loop voltage evolution, shown in Fig. 9, between scenario transition are attributed to the sudden decrease of the bootstrap current arising from the sudden decrease of electron temperatures and their gradients due to the decrease of the ICRH power. In order to compensate for the loss of the bootstrap current and keep the plasma current constant, the ohmic current increases in response to the loop voltage, $U_{loop}$, delivered by the plasma current controller. Therefore, $U_{loop}$ transiently increases before it is reduced to about 0 on a longer time scale due to the growth of $P_{LHCD}$ and of the associated LH driven current, which leads to an increase of the central safety factor and shear reversal.Even though it plays a negligible role in the steady state scenarios, the ohmic current can
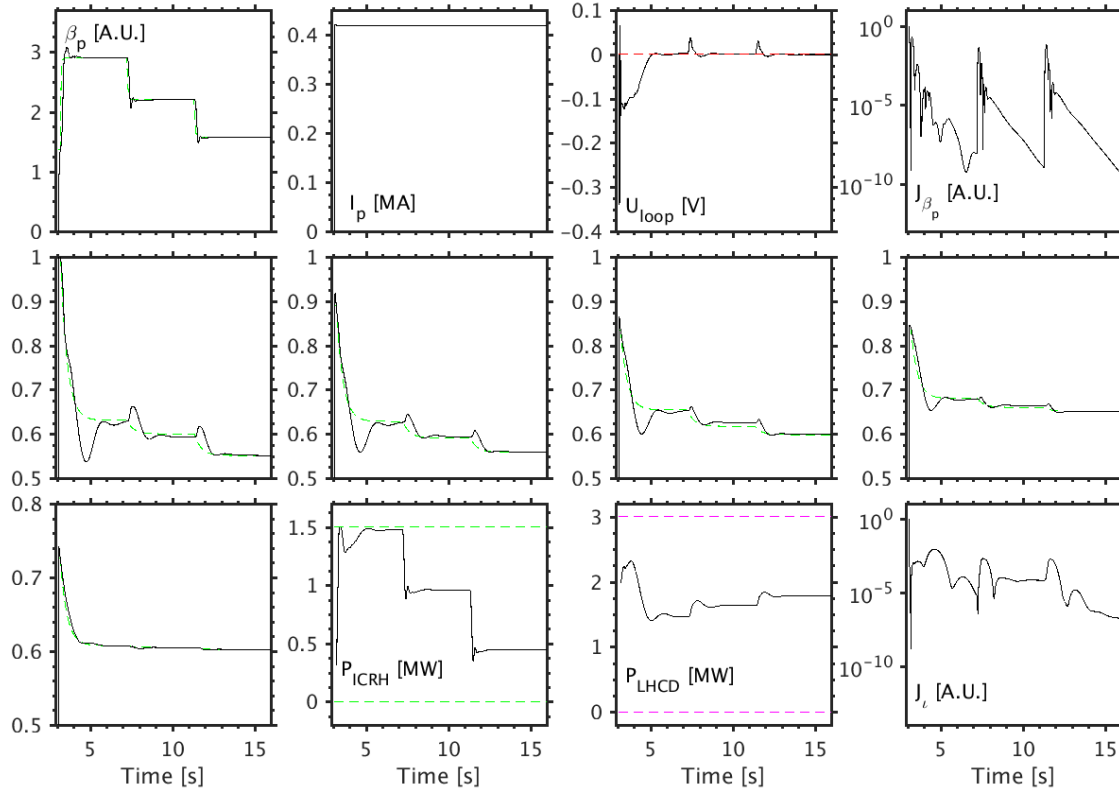
27

Figure 8: Tracking of $\iota$ points at 0, 0.1, 0.2, ..., 0.4 and $\beta_p$ simultaneously. Top panels from left to right: time traces of plasma poloidal pressure $\beta_p$, plasma current $I_p$, the loop voltage $U_{\text{loop}}$ (black solid) with the zero loop voltage line (red dashed) , the averaged relative error for $\beta_p$, $\langle J_{\beta_p} \rangle$. Middle panels from left to right: time traces of the $\iota$ setpoints (green dashed) and evolutions (black solid) at x = 0, 0.1, 0.2, 0.3. Bottom panels from left to right: time traces of the $\iota$ setpoints (green dashed) and evolutions (black solid) at x = 0.4, the actuated ICRH power $P_{\text{ICRH}}$ (black solid) associated with its power limits (green dashed), the LHCD power $P_{\text{LHCD}}$ (black solid) associated with its power limits (magenta dashed), and the averaged relative error for $\iota$, $\langle J_\iota \rangle$.

be used transiently after setpoint changes or plasma disturbances considering the different time scales in which various parameters such as the bootstrap current or the LH driven current evolve.

390   *4.2. Tracking with moderate time delays and power saturations*

In this sub-section, we first present the METIS simulation results with different levels of time delays. Then comparison of the simulations with and without the control conditioning module is
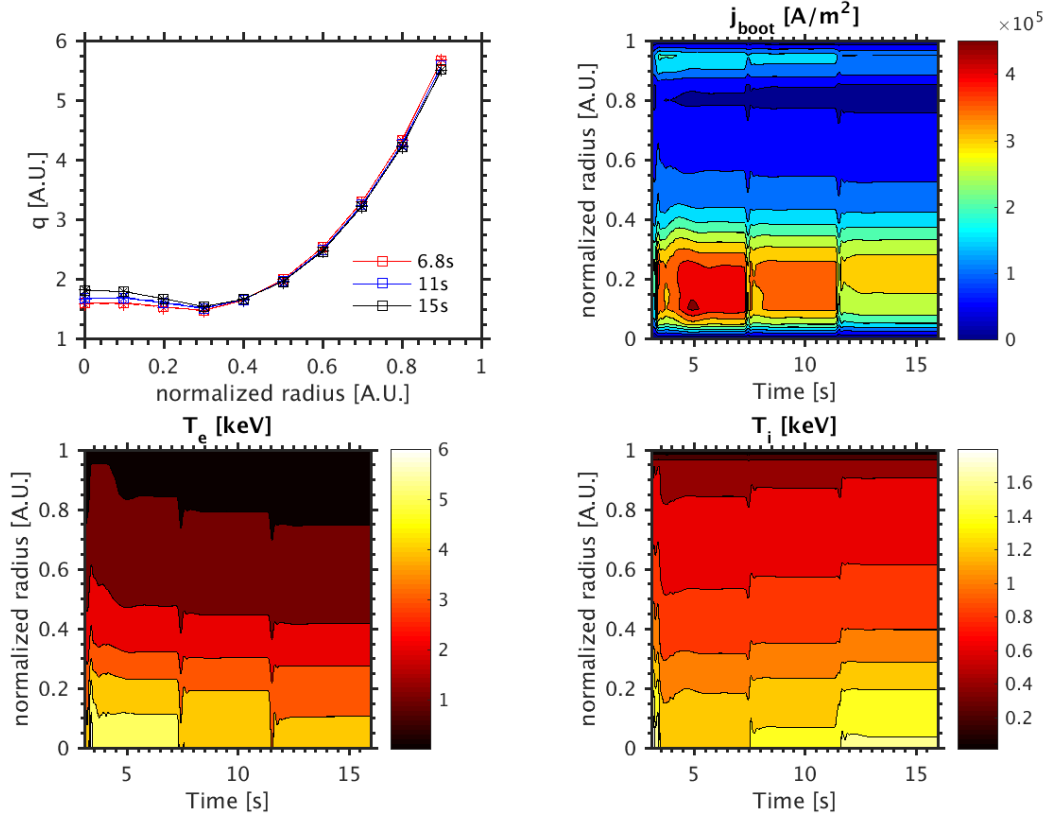
28

Figure 9:  Simulation of a steady-state scenario. Left-top panel: typical q-profile setpoints (asterisk and dashed) and evolutions (square and solid) at 6.8 s (red), 11 s (blue) and 15 s (black). Right-top panel: contour plot of the bootstrap current $j_{boot}$ evolution. Left-bottom panel: contour plot of the electron temperature profile $T_e$ evolution. Right-bottom panel: contour plot of the ion temperature profile $T_i$ evolution.

provided to highlight the importance of online control conditioning for the feedback controller in attenuating the negative effects from time delays and power saturations.

<sup>395</sup> Basically, the tokamak operation system is a time delay system, in which the time delays may arise from the PCS sampling, filtering, communication with the associated systems, the actuator systems, the diagnostic systems and the real-time equilibrium reconstruction algorithm. For time delay systems, the effects from time delays can be neglected if they are under a particular threshold. However, exceeding the threshold may result in undesirable oscillations, sometimes even inducing <sup>400</sup> control instability. Since the profile control sampling time is fixed at 20 ms, the time delays that

29

appear in the discrete profile controller should be a multiple of the profile control sampling time. The actuation and measurement time delays can be as small as 1 ms because their sampling frequencies are much larger, e.g. 1000 Hz. The PCS profile control algorithm and the equilibrium reconstruction algorithm with larger sampling time at 20 ms thus constitute a primary source of time delays, which may cause the time delays as large as 20 ms, 40 ms and even 60 ms. In this study, we evaluate the performance of the controller under the time delay environment by artificially varying the time delays in the actuation dynamics at 20 ms, 40 ms and 60 ms respectively. The simulation results are illustrated in Fig. 10. By comparing the evolution of $\beta_p$ and $\iota$ values in the plasma core with the actuation time delays at 20 ms, 40 ms and 60 ms, we can conclude that the control performance is not obviously damaged with the increase of time delays, which is beneficial from the online control conditioning for the controller states using the values of the control commands provided by the controller and of the actual powers provided by the ICRH and LHCD power systems.

Normally, under ideal circumstances if the reference trajectories are properly prescribed, the magnitude and power rate limits of the ICRH and LHCD systems are never violated. However, unpredictable disturbances in tokamak plasmas could drive the plasma to abnormal states, which can probably cause power saturations, sometimes accompanied with time delays. In order to identify whether the controller with online control conditioning can effectively attenuate the effects from both the power saturations and time delays, control performance with and without the anti-windup module are compared in Fig. 11. In the scenario without control conditioning imposed, there are obvious oscillations of the $\beta_p$ evolution at the beginning, which is caused by oscillations of the ICRH power mainly due to 60 ms time delays (i.e. 3 $T_s$). At 7.1 s, the $\beta_p$ setpoints are increased from 2.0 to 3.5 exponentially. However, since the highest ICRH power that can be provided can not support the achievement of $\beta_p$ at 3.5, the ICRH power is saturated until 11.2 s. Then the reference trajectory starts to decrease from 3.5 to 3.0: one can notice that the $\beta_p$ value immediately follows the reference trajectory for the scenario with control conditioning, but the scenario without control conditioning can not respond accordingly for as long as 4 s. As for $\iota$ one can notice that at the beginning the relative errors, i.e. $J_\iota[k]$, for two scenarios are approximately consistent, because the $\iota$ controller does not respond to the high frequency references/disturbances. After the saturation is relaxed, the relative error for $\iota$ with control conditioning is obviously much smaller than the one without control conditioning.

To sum up, using the controller outputs and the actual power measurements, we can calculate
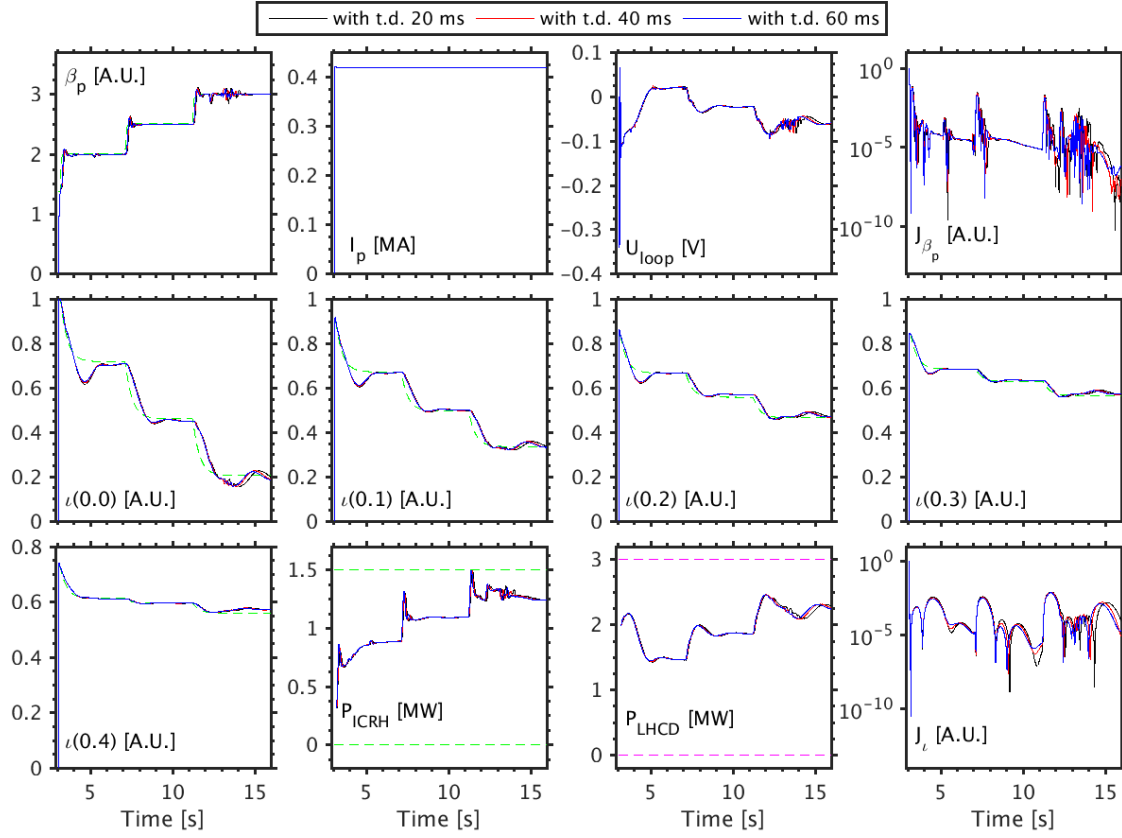
Figure 10: Tracking with the time delays (t.d.) at 20 ms (black), 40 ms (red) and 60 ms (blue). Top panels from left to right: time traces of plasma poloidal pressure $\beta_p$, plasma current $I_p$, the loop voltage $U_{\mathrm{loop}}$, the $\beta_p$ performance index $J_{\beta_p}$. Middle panels from left to right: time traces of the $\iota$ points at $\mathrm{x} = 0$, 0.1, 0.2, 0.3. Bottom panels from left to right: time traces of the $\iota$ point at $\mathrm{x} = 0.4$, the actuated ICRH power $P_{\mathrm{ICRH}}$, the LHCD power $P_{\mathrm{LHCD}}$, and the $\iota$ performance index $J_\iota$. The reference trajectories for $\iota$ and $\beta_p$ are denoted by green dashed lines, the power limits for the ICRH and LHCD are indicated by blue and magenta dashed lines, respectively.

the actuation errors due to power saturations or time delays with respect to the control commands based on the two-time-scale plasma model. Then these errors are fed back to the controller for control states conditioning. This technique can attenuate negative effects from long time delays, e.g. 60 ms, and from the evolution after the power saturations are relaxed.
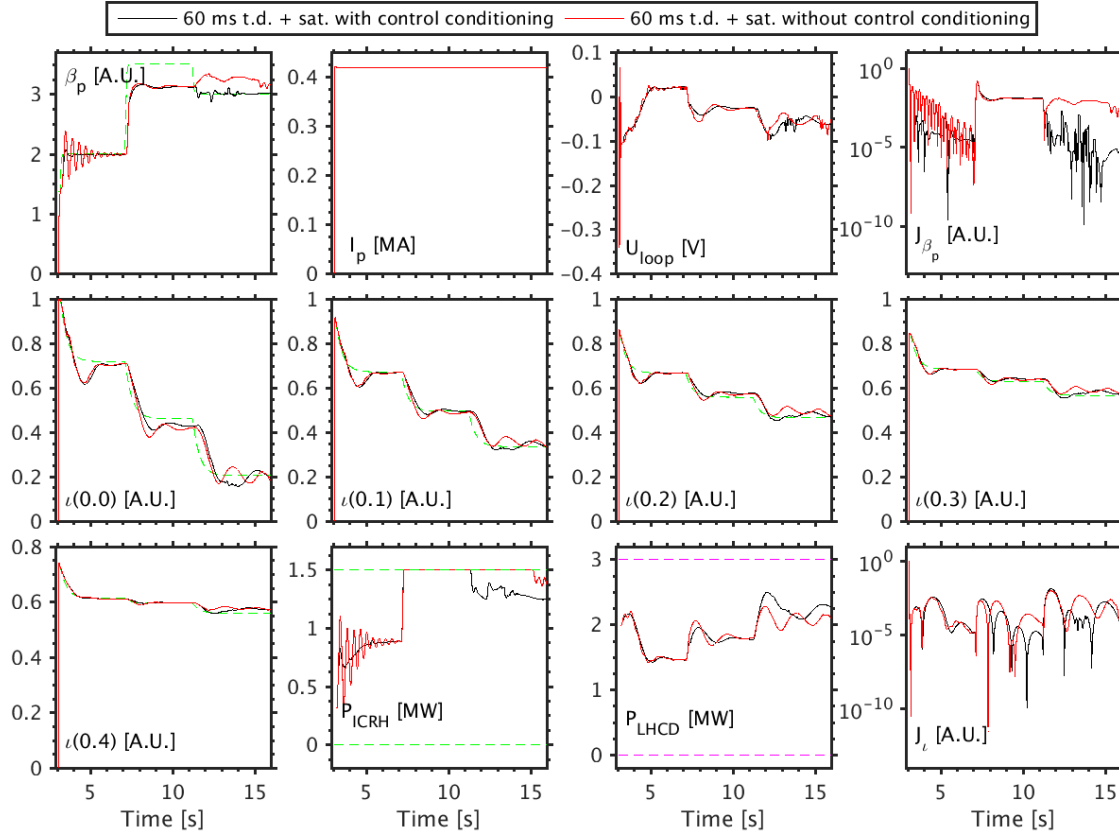
31

Figure 11: Comparison of tracking with 60 ms of time delays (t.d.) plus power saturations with (black solid) and without (red solid) online control conditioning. Top panels from left to right: time traces of plasma poloidal pressure $\beta_p$, plasma current $I_p$, the loop voltage $U_{loop}$, the $\beta_p$ performance index $J_{\beta_p}$. Middle panels from left to right: time traces of the $\iota$ points at x = 0, 0.1, 0.2, 0.3. Bottom panels from left to right: time traces of the $\iota$ point at x = 0.4, the actuated ICRH power P$_{\text{ICRH}}$, the ICRH power P$_{\text{LHCD}}$, and the $\iota$ performance index $J_{\iota}$. The reference trajectories for $\iota$ and $\beta_p$ are denoted by green dashed lines, the power limits for the ICRH and LHCD are indicated by blue and magenta dashed lines respectively.

### 4.3. Tracking with varying weighting functions

The objective of this sub-section is to compare the closed-loop simulation results using the feedback controller tuned with various weighting functions. 6 simulation scenarios were evaluated, whose results are listed in Table 3. All the simulation scenarios have achieved the simultaneous control of the q-profile and $\beta_p$, implying the potential robustness of the feedback controller to the weighting function parameters.

32

Table 3: Weighting functions for the fast $\beta_p$, the slow $\beta_p$ and the $\iota$ local controllers design and performance indexes

| Option | Index | $\omega_{B,\beta_p,F}$ | $\omega_{B,\beta_p,S}$ | $\omega_{B,\iota}$ | $A_{\beta_p,F}$ | $A_{\beta_p,S}$ | $A_\iota$ | - | - | - | - | $\langle \vec{t_r} \rangle$ [s] | $\langle \vec{l}_{os} \rangle$ [%] | $\langle \vec{J} \rangle \times 10^4$ [A.U.] |
|---|---|---|---|---|---|---|---|---|---|---|---|---|---|---|
| | a | $2\pi$ | $\pi$ | $\pi$ | $10^{-5}$ | $10^{-5}$ | $10^{-5}$ | - | - | - | - | (0.107,0.808) | (4.02,3.43) | (9.78,14.0) |
| I | b | $3\pi$ | $1.5\pi$ | $1.5\pi$ | $10^{-5}$ | $10^{-5}$ | $10^{-5}$ | - | - | - | - | (0.0933,0.771) | (5.12,3.80) | (9.09,13.0) |
| | c | $4\pi$ | $2\pi$ | $2\pi$ | $10^{-5}$ | $10^{-5}$ | $10^{-5}$ | - | - | - | - | (0.100,0.752) | (6.19,4.12) | (8.94,12.0) |
| | | $\omega_{B,\beta_p,F}$ | $\omega_{p,\beta_p,S}$ | $\omega_{u,\iota}$ | $\omega_{p,3}$ | $\omega_{u,\iota}$ | $A_{\beta_p,F}$ | $A_{p,\beta_p,S}$ | $A_{u,\beta_p,S}$ | $A_{p,\iota}$ | $A_{u,\iota}$ | | | |
| | d | $2\pi$ | $10^{-0.3}$ | $1$ | $10^{-0.3}$ | $1$ | $10^{-5}$ | $10^{-4.5}$ | $10^{0.1}$ | $10^{-4.5}$ | $10^{0.1}$ | (0.113,1.11) | (1.44,3.47) | (9.96,30.0) |
| II | e | $3\pi$ | $10^{-0.15}$ | $1.2$ | $10^{-0.15}$ | $1.2$ | $10^{-5}$ | $10^{-5.25}$ | $10^{0.1}$ | $10^{-5.25}$ | $10^{0.1}$ | (0.0933,0.906) | (3.33,4.46) | (9.12,26.0) |
| | f | $4\pi$ | $10^{-0.10}$ | $1.5$ | $10^{-0.3}$ | $1.5$ | $10^{-5}$ | $10^{-6}$ | $10^{0.2}$ | $10^{-6}$ | $10^{0.2}$ | (0.0933,0.885) | (4.69,5.18) | ( 9.01,26.0) |

NOTE: $\langle \vec{t_r} \rangle := (\langle t_{r,\beta_p} \rangle, \langle t_{r,\iota} \rangle)$, $\langle \vec{l}_{os} \rangle := (\langle l_{os,\beta_p} \rangle, \langle l_{os,\iota} \rangle)$, $\langle \vec{J} \rangle := (\langle J_{\beta_p} \rangle, \langle J_\iota \rangle)$.

In the scenarios a-c, all three local controllers are tuned with the weighting functions as listed in the option I of Table 1. The tuning parameters $M$ and $A$ are respectively kept at 2 and $10^{-5}$, and the desired closed-loop bandwidths are increased from the scenario a to c. Results show that the performance indexes $\langle \vec{t_r} \rangle$ and $\langle \vec{J} \rangle$ are gradually descreased for both $\beta_p$ and $\iota$ tracking, which is accompanied with the increase of the overshoot index $\langle \vec{l}_{os} \rangle$. In the scenarios d-f, the fast $\beta_p$ controller is tuned with the weighting functions in the Option I, while the slow $\beta_p$ and $\iota$ controllers are tuned with the weighting functions in the Option II. Likewise, the tuning parameter $M$ is fixed at 2 for all the weighting functions, while the desired closed-loop bandwidths and the low frequency tuning parameters are varied. Results imply that with the increase of the desired closed-loop bandwidths, the transient control performance is improved because the performance indexes $\langle \vec{t_r} \rangle$ and $\langle \vec{J} \rangle$ are decreased gradually and the overshoot index $\langle \vec{l}_{os} \rangle$ is increased in the scenarios d-f. In addition, statistics show that the averaged rise time $\langle t_{r,\beta_p} \rangle$, lies in 90-132 ms, i.e. (2.5-3.5) $\tau_E$ and also 4.5-6.6 times the sampling interval, which is physically reasonable and is a tradeoff between the control performance and robustness. The robustness performance to parameter disturbances will be evaluated in the next section.

Comparing the scenarios a-f, we conclude that when using the option II for control design, the $\iota$ control can be improved slightly, but the $\beta_p$ control performance is damaged. To sum up, the tuning of the desired closed-loop bandwidths is essential for the control performance, which should be carefully considered. In addition, the tuning parameter $A$ should be made small, for example, at $10^{-5}$ to guarantee small tracking errors.

In tokamak experiments, there are numerous parameters/profiles that were assumed to be constant but possibly vary and influence, in different degrees, the values of safety factors and plasma pressures. For example the line averaged density $\langle \bar{n}_e \rangle$, the confinement enhancement factor $H_{98}(y, 2)$ and the ion effective charge number $Z_{\text{eff}}$ are among the most important ones. Hence, we consider those quantities as the sources of typical disturbances that occur in the course of the simulation and evaluate the robustness of the closed-loop system. Plasma current disturbances are not taken into account in this study because the plasma current is tightly regulated separately through a dedicated controller.

Simulation results of disturbance rejection by the $\beta_p$ controller are depicted in Fig. 12, where 18 squared wave disturbances emerge in separate periods of the whole simulation as listed in Table 4. Specifically, the value of the averaged density is increased by 30% at 3.6 s ($\beta_p$ at 2), 6.22 s ($\beta_p$ at 2.5) and 8.74 s ($\beta_p$ at 3) respectively and remains constant for 0.5 s before it returns to the original value. The value of the averaged density is decreased by 30% suddenly at 19.82 s ($\beta_p$ at 2.0), 22.34 s ($\beta_p$ at 2.5) and 24.86 s ($\beta_p$ at 3) and remains the same for 0.5 s before returning to the initial value. The H factor is artificially decreased by 30% in the time periods [4.7, 5.2] s, [7.22, 7.72] s and [9.74, 10.24] s, while in the time periods [11.26, 11.76] s, [13.78, 14.28] s and [16.30, 16.80] s it grows by 30%. During the time intervals [12.26, 12.76] s, [17.30, 17.80] s and [21.34, 21.84] s we respectively increase the effective charge number by 30% while during the time intervals [14.78, 15.28] s, [18.82, 19.32] s and [21.34, 21.84] s the effective charge number is decreased by 30 %. We can conclude from our simulations that, in addition to good reference tracking, the fast and slow controllers are as well able to reject the 30% changes of $\bar{n}_e$, $H_{98}(y, 2)$ and $Z_{\text{eff}}$ with a response time at around 0.25 s when the ICRH power is not saturated. We note that if the upper limit of the ICRH power is 1.5 MW, it is not possible to reject the 30% decrease of $H_{98}(y, 2)$ when $\beta_p$ is over 2.5 and also it cannot reject 30 % decrease of $\bar{n}_e$ and $Z_{\text{eff}}$ when $\beta_p$ is at 3. The reason is that under those conditions the available ICRH power is not able to compensate the reduced part of $\beta_p$ arising from the decrease of $H_{98}(y, 2)$, $\bar{n}_e$ and/or $Z_{\text{eff}}$. Importantly, we highlight that among all three parameters, $H_{98}(y, 2)$ is the most important parameter that can significantly affect $\beta_p$.

The robustness test of the $\iota$ controller against typical squared wave disturbances is presented in Fig. 13. In this case, three squared wave disturbances are imposed in the periods of [4, 4.5] s (30% increase of $\bar{n}_e$), [8, 8.5] s (30% increase of $H_{98}(y, 2)$)and [12, 12.5] s (30% increase of $Z_{\text{eff}}$).

34

Table 4: List of the parameter variations

| $\beta_p$ | $\delta\bar{n}_e$ [%], T.I. [s] | $\delta H_{98}(y,2)$[%], T.I. [s] | $\delta Z_{\mathrm{eff}}$ [%], T.I. [s] |
|---|---|---|---|
| 2 | +30 %, [3.7, 4.2] | +30%, [11.26, 11.76] | +30%, [12.26, 12.76] |
| | -30 %, [19.82, 20.32] | -30%, [4.7, 5.2] | -30%, [14.78, 15.28] |
| 2.5 | +30%, [6.22, 6.72] | +30%, [13.78, 14.28] | +30%, [17.30, 17.80] |
| | -30%, [22.34, 22.84] | -30%, [7.22, 7.72] | -30%, [18.82, 19.32] |
| 3 | +30%, [8.74, 9.24] | +30%, [16.30, 16.80] | +30%, [21.34, 21.84] |
| | -30%, [24.86, 25.36] | -30%, [9.74, 10.24] | -30%, [23.86, 24.36] |

Even though the simulation experienced large and sudden disturbances in the first two phases, two groups of setpoints are finally reached without exceeding the limits of ICRH and LHCD powers. As for the third phase, since the model mistmatches are enlarged with strongly negative magnetic shear due to nonlinearity, the setpoints are reached after a few oscillations.

The simultaneous control of $\iota$ at 0, 0.1, 0.2, ..., 0.5 and $\beta_p$ with typical disturbances is shown in Fig. 14. There are three squared wave disturbances with the amount of 30% growth occurring in the time intervals [4, 4.5] s (for averaged density), [8, 8.5] s (for H factor) and [12, 12.5] s (for effective charges). In addition to reference tracking, $\beta_p$ is well regulated against the three sudden and large disturbances with a response time of 0.2 s. The $\iota$ controller is able to reject the disturbances of both H factor and plasma density and finally reaches the targets. For the strongly negative shear case, it takes more time to achieve the target since the model mismatches are much larger, but it is nevertheless approached as closely as possible. Note that when $\beta_p$ is at 3.0, a large amount of ICRH power is needed to sustain this value and only a limited amount of power is left to reject the disturbance, thus the ICRH power is saturated between 12 s and 12.5 s.

## 5. Conclusion and Outlook

In this work, a new $\mathcal{H}_\infty$ robust controller has been developed for the tracking of the safety factor profile and the poloidal plasma pressure parameter, based on a two-time-scale data-driven model. The model is divided into 3 sub-models for separate control synthesis and eventually all the local controllers are combined for composite feedback control. In order to attenuate the negative effects from power saturations and time delays, a controller states conditioning loop is utilized to compensate for the actuation errors due to power saturation and time delays. Meanwhile, to avoid undesirable bumps, overshoots and power saturations at the control initialization, some pre-
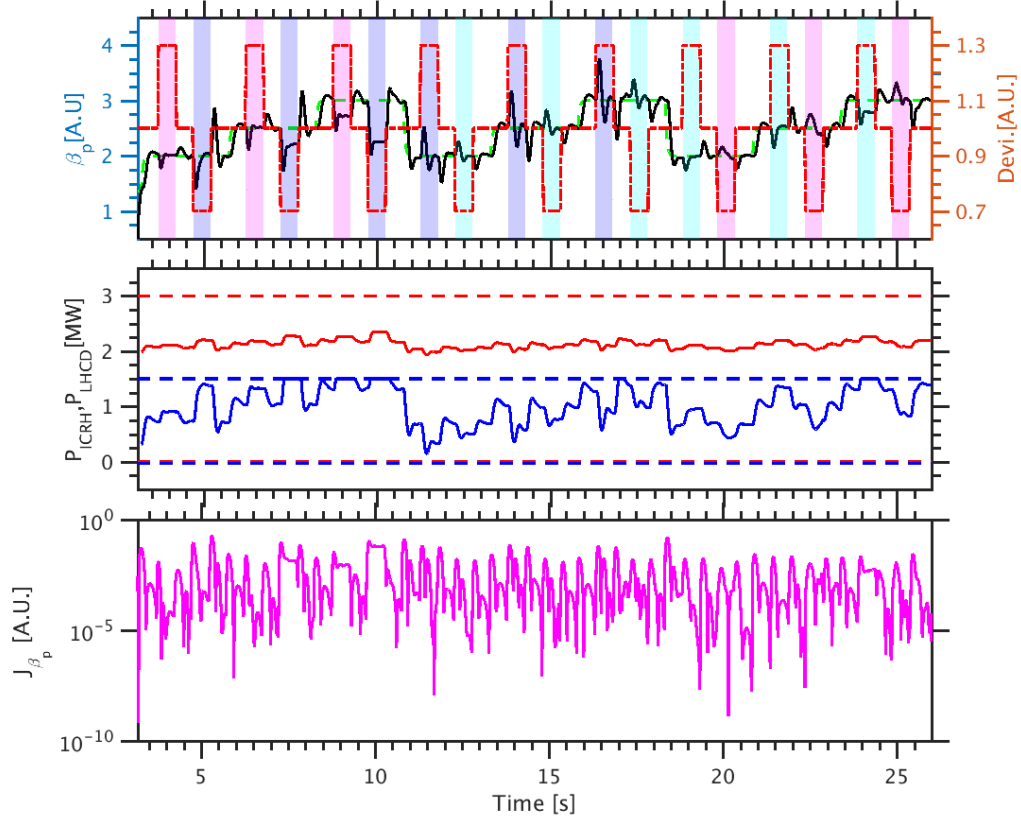
35

Figure 12: Disturbance rejection of $\beta_p$ control. Top panel: time traces of $\beta_p$ setpoints (green dashed) and evolutions (black solid), with the associated parameter variation intervals: magenta areas indicate that $\bar{n}_e$ is activated as a parameter disturbance, while $H_{98}(y,2)$ corresponds to the light purple areas and $Z_{\text{eff}}$ is linked with cyan areas. The red dotted line represents the relative variation of each activated disturbance parameter. Middle panel: time traces of actuated powers $P_{ICRH}$ (blue solid) and $P_{LHCD}$ (red solid), as well as power ranges of ICRH (blue dashed) and LHCD (red dashed). Bottom panel: time traces of the relative error for $\beta_p$, i.e. $J_{\beta_p}$.

515 configurations on the setpoints and pre-filters are carefully made. The control tunings and relevant control performance have been evaluated numerically to provide some indications on experimental control tunings for the robust feedback controller. Importantly, extensive nonlinear closed-loop simulations with the METIS code show that using LHCD@4.6GHz and ICRH@33MHz systems as control actuators the proposed controller can successfully achieve and regulate the monotonic 520 q-profile and reversed magnetic shear with high $\beta_p$ in H-mode steady-state scenarios on EAST.
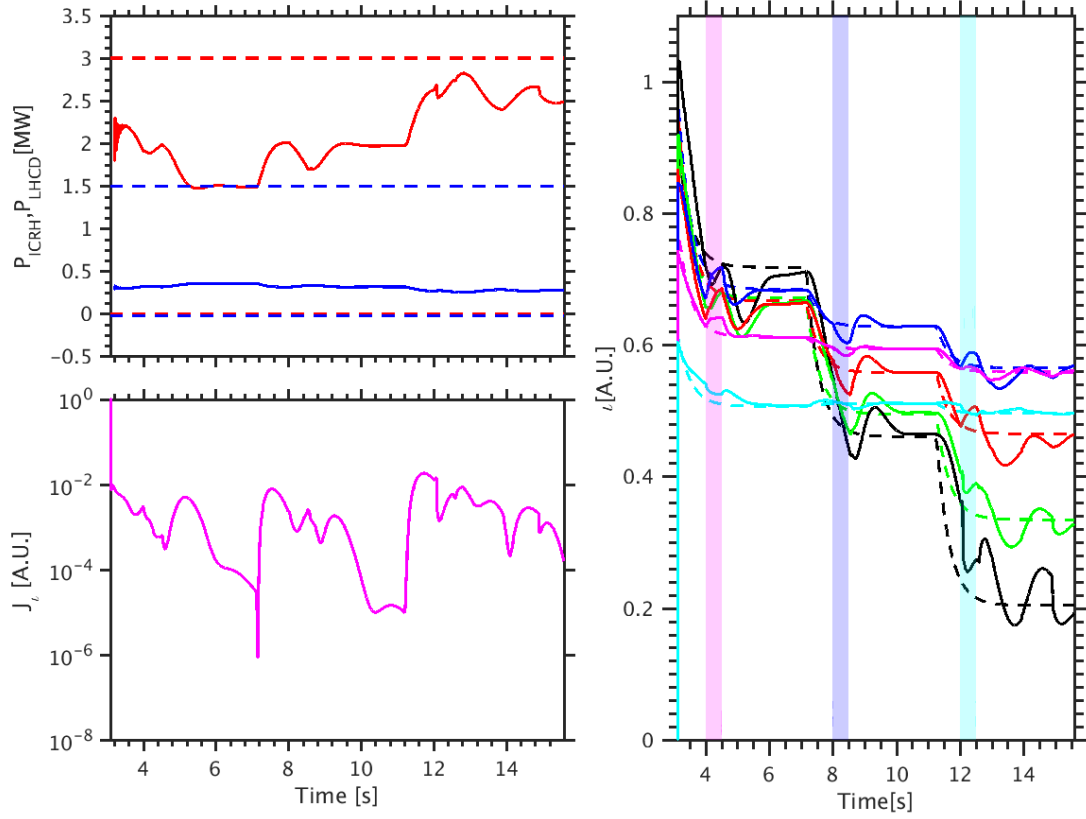
36

Figure 13: Disturbance rejection of $\iota$ control. Left-top panel: time traces of actuated powers $P_{ICRH}$ (blue) and $P_{LHCD}$ (red), power ranges of ICRH (blue dash) and LHCD (red dash). Left-bottom panel: time traces of the averaged relative error index for $\iota$. Right panel: time traces of $\iota$ values (solid) and setpoints (dashed) at x = 0 (black), 0.1 (green), 0.2 (red), 0.3 (blue), 0.4 (magenta), 0.5 (cyan) with $\iota$ feedback control. Magenta, light purple and cyan areas are respectively indicating 30 % increase of $\bar{n}_e$, $H_{98}(y,2)$ and $Z_{eff}$.

Robustness tests indicate that it is possible to maintain the states by rejecting the disturbances of up to different levels of plasma density variation, H-factor variation and effective charge variation separately.

In the future, the implementation of the control algorithms into the EAST plasma control system is expected and experimental tests on EAST are foreseen to further validate the effectiveness of the proposed control scheme. Furthermore, a series of extensions can be made based on the proposed controller. Firstly, control adaptivity can be imposed on the feedback controller (treated as a central
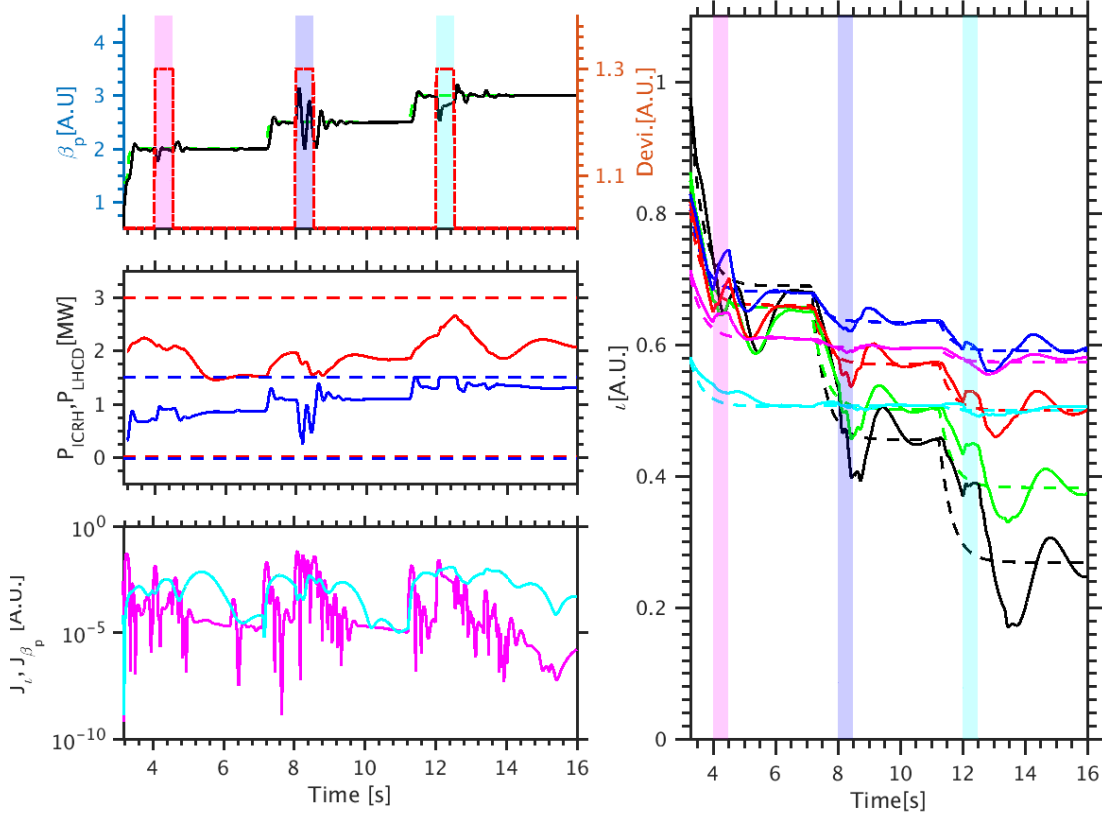
37

Figure 14: Disturbance rejection of simultaneous $\iota$ and $\beta_p$ control. Left-top panel: time traces of $\beta_p$ setpoints (green dashed) and evolutions (black), with magenta, light purple and cyan areas respectively indicating 30 % increase of $\bar{n}_e$, $H_{98}(y,2)$ and $Z_{\text{eff}}$. Left-middle panel: time traces of actuated powers $P_{\text{ICRH}}$ (blue solid) and $P_{\text{LHCD}}$ (red solid), power limits of ICRH (blue dashed) and LHCD (red dashed). Left-bottom panel: time traces of the relative error for $\iota(x)$ (cyan solid) on x and $\beta_p$ (magenta solid). Right panel: time traces of $\iota$ values (solid) and setpoints (dashed) at x = 0 (black), 0.1 (green), 0.2 (red), 0.3 (blue), 0.4 (magenta), 0.5 (cyan) with $\iota$ feedback control.

controller) to enhance its control performance, for example, reducing the overshoots and steady-state errors, especially for the fast timescale kinetic control and the central safety factor control. In addition, a plant model-based feedforward can be combined with the feedback controller to not only actively control the response time but also optimally reduce the transient errors between measurements/estimations and setpoints, while the disturbance model-based feedforward can be implemented to deal with typical disturbances at the timescale beyond the control bandwidth of the fast controller. It is also interesting to explore the high plasma current, high plasma pressure,
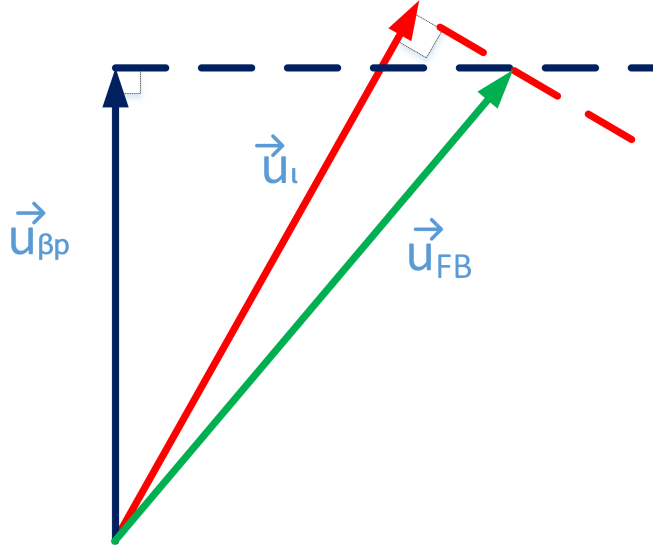
38

Figure A.1:   Geographic illustration

high bootstrap current fraction steady-state scenarios with the inclusion of neutral beam injection (NBI) and electron cyclotron current drive (ECCD) as control actuators for the integrated control of the safety factor profile, ion temperature and plasma rotation profiles and MHD instabilities.

**Acknowledgements**

## Appendix A. Derivation of the decoupling coefficients

As shown in Fig. A.1., to calculate the decoupling coefficients, the following conditions should be satisfied:

$$\vec{u}_{FB} \cdot \frac{\vec{u}_{\beta_p}}{\|\vec{u}_{\beta_p}\|} = \|\vec{u}_{\beta_p}\|, \vec{u}_{FB} \cdot \frac{\vec{u}_{\iota}}{\|\vec{u}_{\iota}\|} = \|\vec{u}_{\iota}\| \tag{A.1}$$

Combining equations (A.1) and (15), we can derive:

$$
\begin{aligned}
\lambda_{\beta_p}\|\vec{u}_{\beta_p}\|^2 + \lambda_{\iota}\vec{u}_{\iota} \cdot \vec{u}_{\beta_p} &= -\vec{u}_{\iota} \cdot \vec{u}_{\beta_p} \\
\lambda_{\iota}\|\vec{u}_{\iota}\|^2 + \lambda_{\beta_p}\vec{u}_{\beta_p} \cdot \vec{u}_{\iota} &= -\vec{u}_{\beta_p} \cdot \vec{u}_{\iota}
\end{aligned}
\tag{A.2}
$$

Solving equations (A.2), we obtain the decoupling coefficients $\lambda_{\beta_p}$ and $\lambda_{\iota}$ as follows:

$$\lambda_{\beta_p} = \frac{\left(\frac{\vec{u}_{\iota} \cdot \vec{u}_{\beta_p}}{\|\vec{u}_{\iota}\|\|\vec{u}_{\beta_p}\|}\right)^2 - \frac{\vec{u}_{\iota} \cdot \vec{u}_{\beta_p}}{\|\vec{u}_{\beta_p}\|^2}}{1 - \left(\frac{\vec{u}_{\iota} \cdot \vec{u}_{\beta_p}}{\|\vec{u}_{\iota}\|\|\vec{u}_{\beta_p}\|}\right)^2}, \lambda_{\iota} = \frac{\left(\frac{\vec{u}_{\beta_p} \cdot \vec{u}_{\iota}}{\|\vec{u}_{\beta_p}\|\|\vec{u}_{\iota}\|}\right)^2 - \frac{\vec{u}_{\beta_p} \cdot \vec{u}_{\iota}}{\|\vec{u}_{\iota}\|^2}}{1 - \left(\frac{\vec{u}_{\beta_p} \cdot \vec{u}_{\iota}}{\|\vec{u}_{\beta_p}\|\|\vec{u}_{\iota}\|}\right)^2}$$

## References

[1] J. Wesson, D. J. Campbell, Tokamaks, Vol. 149, Oxford University Press, 2011.

[2] C. Kessel, J. Manickam, G. Rewoldt, W. Tang, Improved plasma performance in tokamaks with negative magnetic shear, Physical Review Letters 72 (8) (1994) 1212.

[3] D. Humphreys, G. Ambrosino, P. de Vries, F. Felici, S. H. Kim, G. Jackson, A. Kallenbach, E. Kolemen, J. Lister, D. Moreau, et al., Novel aspects of plasma control in ITER, Physics of Plasmas 22 (2) (2015) 021806.

[4] R. E. Denton, J. Drake, R. G. Kleva, D. Boyd, Skin currents and compound sawteeth in tokamaks, Physical Review Letters 56 (23) (1986) 2477.

[5] E. Westerhof, O. Sauter, M. Mayoral, D. Howell, M. Mantsinen, M. Nave, B. Alper, C. Angioni, P. Belo, R. Buttery, et al., Control of sawteeth and triggering of NTMs with ion cyclotron resonance frequency waves in JET, Nuclear fusion 42 (11) (2002) 1324.

[6] R. Wolf, Internal transport barriers in tokamak plasmas, Plasma Physics and Controlled Fusion 45 (1) (2002) R1.

[7] K. Ida, T. Fujita, Internal transport barrier in tokamak and helical plasmas, Plasma Physics and Controlled Fusion 60 (3) (2018) 033001.

[8] D. Moreau, M. L. Walker, J. R. Ferron, F. Liu, E. Schuster, J. E. Barton, M. D. Boyer, K. H. Burrell, S. Flanagan, P. Gohil, et al., Integrated magnetic and kinetic control of advanced tokamak plasmas on DIII-D based on data-driven models, Nuclear Fusion 53 (6) (2013) 063020.

[9] J. E. Barton, K. Besseghir, J. Lister, E. Schuster, Physics-based control-oriented modeling and robust feedback control of the plasma safety factor profile and stored energy dynamics in ITER, Plasma Physics and Controlled Fusion 57 (11) (2015) 115003.

[10] J. E. Barton, M. D. Boyer, W. Shi, W. Wehner, E. Schuster, J. R. Ferron, M. L. Walker, D. A. Humphreys, T. C. Luce, F. Turco, et al., Physics-model-based nonlinear actuator trajectory optimization and safety factor profile feedback control for advanced scenario development in DIII-D, Nuclear Fusion 55 (9) (2015) 093005.

[11] E. Schuster, W. P. Wehner, J. E. Barton, M. D. Boyer, T. C. Luce, J. R. Ferron, C. T. Holcomb, M. L. Walker, D. A. Humphreys, W. M. Solomon, et al., Enhanced reproducibility of L-mode plasma discharges via physics-model-based q-profile feedback control in DIII-D, Nuclear Fusion 57 (11) (2017) 116026.

[12] M. D. Boyer, J. Barton, E. Schuster, M. L. Walker, T. C. Luce, J. R. Ferron, B. G. Penaflor, R. D. Johnson, D. A. Humphreys, Backstepping control of the toroidal plasma current profile in the DIII-D tokamak., IEEE Trans. Contr. Sys. Techn. 22 (5) (2014) 1725–1739.

[13] J. E. Barton, M. D. Boyer, W. Shi, E. Schuster, T. C. Luce, J. R. Ferron, M. L. Walker, D. A. Humphreys, B. G. Penaflor, R. D. Johnson, Toroidal current profile control during low confinement mode plasma discharges in DIII-D via first-principles-driven model-based robust control synthesis, Nuclear Fusion 52 (12) (2012) 123018.

[14] I. Goumiri, C. Rowley, S. Sabbagh, D. Gates, S. Gerhardt, M. Boyer, R. Andre, E. Kolemen, K. Taira, Modeling and control of plasma rotation for NSTX using neoclassical toroidal viscosity and neutral beam injection, Nuclear Fusion 56 (3) (2016) 036023.

[15] I. Goumiri, C. Rowley, S. Sabbagh, D. Gates, M. Boyer, S. Gerhardt, E. Kolemen, J. Menard,

Simultaneous feedback control of plasma rotation and stored energy on NSTX-U using neoclassical toroidal viscosity and neutral beam injection, Physics of plasmas 24 (5) (2017) 056101.

[16] M. Boyer, R. Andre, D. Gates, S. Gerhardt, I. Goumiri, J. Menard, Central safety factor and betan control on NSTX-U via beam power and plasma boundary shape modification, using TRANSP for closed loop simulations, Nuclear Fusion 55 (5) (2015) 053033.

[17] E. Maljaars, F. Felici, M. De Baar, J. van Dongen, G. Hogeweij, P. Geelen, M. Steinbuch, Control of the tokamak safety factor profile with time-varying constraints using MPC, Nuclear Fusion 55 (2) (2015) 023001.

[18] E. Maljaars, F. Felici, T. Blanken, C. Galperti, O. Sauter, M. De Baar, F. Carpanese, T. Goodman, D. Kim, S. Kim, et al., Profile control simulations and experiments on TCV: a controller test environment and results using a model-based predictive controller, Nuclear Fusion 57 (12) (2017) 126063.

[19] N. M. T. Vu, R. Nouailletas, L. Lefèvre, F. Felici, Plasma q-profile control in tokamaks using a damping assignment passivity-based approach, Control Engineering Practice 54 (2016) 34–45.

[20] B. Mavkov, E. Witrant, C. Prieur, E. Maljaars, F. Felici, O. Sauter, et al., Experimental validation of a Lyapunov-based controller for the plasma safety factor and plasma pressure in the TCV tokamak, Nuclear Fusion 58 (5) (2018) 056011.

[21] B. Mavkov, E. Witrant, C. Prieur, Distributed control of coupled inhomogeneous diffusion in tokamak plasmas, IEEE Transactions on Control Systems Technology (99) (2017) 1–8.

[22] D. Moreau, D. Mazon, M. Ariola, G. De Tommasi, L. Laborde, F. Piccolo, F. Sartori, T. Tala, L. Zabeo, A. Boboc, et al., A two-time-scale dynamic-model approach for magnetic and kinetic profile control in advanced tokamak scenarios on JET, Nuclear Fusion 48 (10) (2008) 106001.

[23] L. Laborde, D. Mazon, D. Moreau, A. Murari, R. Felton, L. Zabeo, R. Albanese, M. Ariola, J. Bucalossi, F. Crisanti, et al., A model-based technique for integrated real-time profile control in the JET tokamak, Plasma Physics and Controlled Fusion 47 (1) (2004) 155.

[24] D. Moreau, F. Crisanti, X. Litaudon, D. Mazon, P. De Vries, R. Felton, E. Joffrin, L. Laborde, M. Lennholm, A. Murari, et al., Real-time control of the q-profile in JET for steady state advanced tokamak operation, Nuclear Fusion 43 (9) (2003) 870.

42

[25] E. Witrant, E. Joffrin, S. Brémond, G. Giruzzi, D. Mazon, O. Barana, P. Moreau, A control-oriented model of the current profile in tokamak plasma, Plasma Physics and Controlled Fusion 49 (7) (2007) 1075.

[26] D. Moreau, D. Mazon, M. Walker, J. Ferron, K. Burrell, S. Flanagan, P. Gohil, R. Groebner, A. Hyatt, R. La Haye, et al., Plasma models for real-time control of advanced tokamak scenarios, Nuclear Fusion 51 (6) (2011) 063009.

[27] D. Moreau, J. Artaud, J. R. Ferron, C. T. Holcomb, D. A. Humphreys, F. Liu, T. C. Luce, J. M. Park, R. Prater, F. Turco, et al., Combined magnetic and kinetic control of advanced tokamak steady state scenarios based on semi-empirical modelling, Nuclear Fusion 55 (6) (2015) 063011.

[28] J. Artaud, F. Imbeaux, J. Garcia, G. Giruzzi, T. Aniel, V. Basiuk, A. Bécoulet, C. Bourdelle, Y. Buravand, J. Decker, et al., METIS: a fast integrated tokamak modelling tool for scenario design, Nuclear Fusion 58 (10) (2018) 105001.

[29] R. Nouailletas, E. Nardon, S. Brémond, Robust vertical plasma stabilization of the future tungsten divertor configuration of Tore Supra, IFAC Proceedings Volumes 47 (3) (2014) 1349–1354.

[30] R. Nouailletas, E. Nardon, P. Moreau, C. Reux, et al., WEST magnetic control, in: 2019 IEEE 58th Conference on Decision and Control (CDC), IEEE, 2019, pp. 3214–3219.

[31] T. Blanken, F. Felici, C. Galperti, O. Kudláček, F. Janky, A. Mlynek, L. Giannone, P. Lang, W. Treutterer, W. Heemels, et al., Model-based real-time plasma electron density profile estimation and control on ASDEX Upgrade and TCV, Fusion Engineering and Design 147 (2019) 111211.

[32] S. Skogestad, I. Postlethwaite, Multivariable feedback control: analysis and design, Vol. 2, Wiley New York, 2007.

[33] C. Scherer, P. Gahinet, M. Chilali, Multiobjective output-feedback control via LMI optimization, IEEE Transactions on automatic control 42 (7) (1997) 896–911.

[34] R. Hanus, M. Kinnaert, J.-L. Henrotte, Conditioning technique, a general anti-windup and bumpless transfer method, Automatica 23 (6) (1987) 729–739.

43

[35] H. Liu, J. Qian, Y. Jie, W. Ding, D. Brower, Z. Zou, W. Li, H. Lian, S. Wang, Y. Yang, et al., Initial measurements of plasma current and electron density profiles using a polarimeter/interferometer (POINT) for long pulse operation in EAST, Review of Scientific Instruments 87 (11) (2016) 11D903.

[36] H. Liu, Y. Jie, W. Ding, D. Brower, Z. Zou, J. Qian, W. Li, Y. Yang, L. Zeng, S. Zhang, et al., Internal magnetic field measurements by laser-based polarimeter-interferometer (POINT) system on EAST, Journal of Instrumentation 11 (01) (2016) C01049.

[37] Y. Huang, B. Xiao, Z. Luo, J. Qian, S. Li, Y. Chen, H. Liu, L. Xu, Y. Yuan, Q. Yuan, Development of real-time plasma current profile reconstruction with POINT diagnostic for EAST plasma control, Fusion Engineering and Design 120 (2017) 1–8.

[38] J. Cordey, K. Thomsen, A. Chudnovskiy, O. Kardaun, T. Takizuka, J. Snipes, M. Greenwald, L. Sugiyama, F. Ryter, A. Kus, et al., Scaling of the energy confinement time with $\beta$ and collisionality approaching iter conditions, Nuclear fusion 45 (9) (2005) 1078.

44